2-1-2012

Two cylindrical vortex sheets : evolution and singularity formation

Johnson Jeremy

Jeremy David Johnson
Candidate

Mathematics
Department

This thesis is approved, and it is acceptable in quality and form for publication:

Approved by the Thesis Committee:

Monika Nitsche — Dr. Monika Nitsche, Chairperson

Pedro J Embid — Dr. Pedro Embid

Jens Lorenz — Dr. Jens Lorenz

Two Cylindrical Vortex Sheets; Evolution and Singularity Formation

by

Jeremy David Johnson

B.S., Mathematics, University of New Mexico, 2007

THESIS

Submitted in Partial Fulfillment of the

Requirements for the Degree of

Master of Science

Mathematics

The University of New Mexico

Albuquerque, New Mexico

May, 2011

Acknowledgments

I wish to thank all of the following from the University of New Mexico: Professor Monika Nitsche, my committee chair, for her substantial amounts of instruction, guidance, patience, and support she has shown me over the years; Professor Pedro Embid, my committee member, for all of the fantastic courses that he has taught, his counsel,, helpful comments, enthusiasm, and especially, his kindness; and Professor Jenz Lorenz, my committee member, for coming on board with short notice. I am very grateful for these and the many other efforts of the named professors.

Two Cylindrical Vortex Sheets; Evolution and Singularity Formation

by

Jeremy David Johnson

ABSTRACT OF THESIS

Submitted in Partial Fulfillment of the
Requirements for the Degree of

Master of Science
Mathematics

The University of New Mexico

Albuquerque, New Mexico

May, 2011

Two Cylindrical Vortex Sheets; Evolution and Singularity Formation

by

Jeremy David Johnson

B.S., Mathematics, University of New Mexico, 2007

M.S., Mathematics, University of New Mexico, 2011

Abstract

Using Rosenhead's point-vortex approximation with correction terms, the evolution of two symmetrical, counter-rotating, initially cylindrical vortex sheets in an incompressible, potential fluid flow is studied. Simulations are performed in time up to the occurrence of branch-point curvature singularities in the vortex sheets' geometries. The numerical methods employed are discussed. Parameters pertaining to the asymptotics of the Fourier coefficients of the vortex sheets' positions are numerically fitted to gain insight into aspects of the singularity formation; these include the order of the branch-point singularities, and the times and locations of singularity formation. A smoothing over initial singularity formations is implemented by either the heat equation or through a local application of the vortex blob method in an attempt to gain details into further singularity formations. Lastly, the effects of the initially prescribed total circulation around the vortex sheets on their evolutions are studied, both up to the time of singularity formation, and with the implementation of the vortex blob method, past the times of singularity formation.

Contents

List of Figures

Glossary

$\mathbf{u}$	Velocity field of the flow.
$\boldsymbol{\xi}$	Vorticity field of the flow.
$\Gamma(\alpha)$	Circulation distribution.
Γ_T	Total circulation distribution around the top vortex sheet.
σ	$= \frac{\partial \Gamma}{\partial s}$. Vortex sheet strength.
ψ	Stream function.
μ	$= \frac{D}{R}$. Non-dimensionalized separation distance between the two cylinders.
$\boldsymbol{\kappa}$	Curvature.
s	Arclength.
l	Corresponds to Fourier filter level 10^{-l}. Filter level may also be referred to by tol.
N	Number of point-vorticies used in approximating either the top or the bottom vortex sheet.

Glossary

α	Lagrangian parameter relating to the positions of the vortex sheets. At t=0 it is the angle from the x-axis to a point on the vortex sheet, taken in the counterclockwise direction.
α_c	Lagrangian parameter corresponding to the location of singularity formation in the vortex sheet.
p	Order of branch-point curvature singularity.
δ	Artificial regularization parameter used in association with the vortex blob method.

Chapter 1

Introduction

1.1 Overview

In this paper, we study the evolution of two symmetrical, counter-rotating, initially cylindrical vortex sheets in an incompressible, potential fluid flow[1]. See schematic given in Figure 1.1. Initially, the fluid within the vortex sheets move with constant velocity $\mathbf{U}$ normal to the plane containing both center lines of the vortex sheets. The flow at infinity is given by $\mathbf{u}_\infty = \mathbf{0}$. The total circulation around each vortex sheet is prescribed. Positive circulation is taken to be counter-clockwise directed.

An almost physical description of our problem can be considered as follows: Suppose that initially two thin, symmetrical, counter-rotating cylindrical metal shells be set in an instantaneous impulsive motion given by a velocity normal to itself while immersed in a stagnant, inviscid, incompressible, irrotational fluid. Let the boundary condition[2] on the cylinders be $\mathbf{u} \cdot \mathbf{n} = \mathbf{U} \cdot \mathbf{n}$, where $\mathbf{u}$ is the velocity field of the

[1]Take $\mathbf{u}$ to be the velocity field of the flow. Then incompressible means that $\nabla \bullet \mathbf{u} = \mathbf{0}$; potential flow means the flow is both irrotational, $\xi = \nabla \times \mathbf{u} = \mathbf{0}$, and inviscid.

[2]A more physical approximation would be that the no slip condition between the fluid

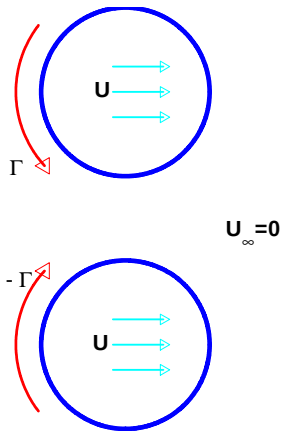

Figure 1.1: Schematic of the symmetrical, counter-rotating, initial cylindrical vortex sheets and associated initial flow.

flow, $\mathbf{U}$ is the velocity vector of both the cylinders and their fluid contained within, and $\mathbf{n}$ is the unit normal to the boundary surfaces.[3] A normal velocity for the flow at the boundary of the cylinders is forbidden. However, at the boundaries, the flow is permitted a tangential velocity to the boundaries. Let the cylindrical walls instantaneously dissolve, and allow the remaining flow to evolve under its self-induced velocity field. The absence of surface tension is assumed in our problem.

Figure 1.2 shows the streamlines for the initial flow, where the reference frame is taken to move with the velocity of flow at infinity given by $\mathbf{u}_\infty = \mathbf{0}$. Figure 1.3 shows the streamlines with a change in the reference frame, which is now taken to move with the cylinders at a velocity $\mathbf{U}$. This latter plot is the same as that for uniform

and the solid boundaries of the cylinders is given by $\mathbf{u} = \mathbf{U}$ on the boundaries of the cylinders [11]. We relax the mentioned condition of no slip so that a tangential velocity at the boundaries is permitted.

[3]The condition $\mathbf{u} \cdot \mathbf{n} = \mathbf{U} \cdot \mathbf{n}$ on the boundaries of the cylinders implies that the surface of the two cylinders must be a streamline [11]. $\mathbf{n}$ is directed outward from the cylinder in consideration

potential flow of velocity $-\mathbf{U}$ given at infinity, past two stationary, counter-rotating cylinders.[4] The reader may be familiar with the well known case of uniform potential flow past one stationary cylinder, for which its complex potential is easily found [11]. Solving for the complex potential in the instances of uniform potential flow past two or more cylinders is not as easy, however. Analytically, Lagally (1929) [16] was one who solved the problem for potential flow past two cylinders with circulations, using tools from elliptic function theory. Crowdy [6] [7] [8] [9] used conformal mappings, the generalized Riemann mapping theorem, and the use of the Schottky-Klein prime function to solve the general problem exactly in terms of infinite products; that is, for the problem of potential flow past a finite number of cylinders with given circulations.

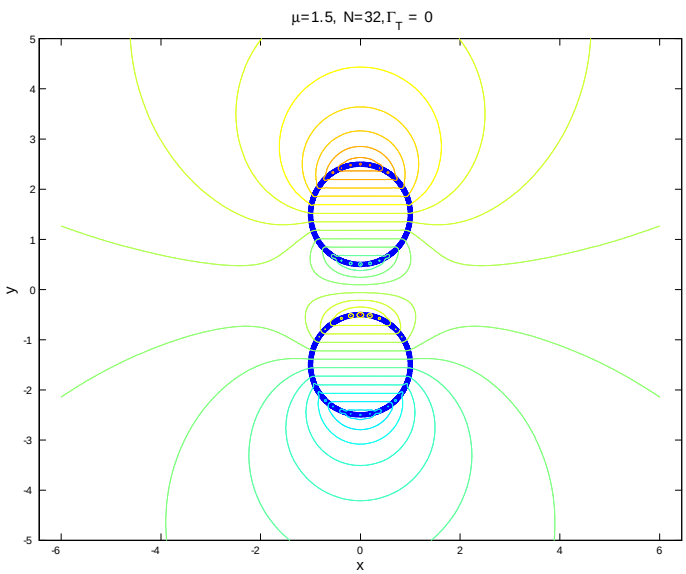

Figure 1.2: Streamlines for the initial flow. The reference frame is taken to move with the flow at $\mathbf{u}_\infty = \mathbf{0}$.

Modelling the evolution of two initially cylindrical vortex sheets is a natural precursor to modelling the evolution of an initially toroidal vortex sheet. Reason

[4] In the figures showing the streamlines, the cylinders were taken to have 0 circulations.

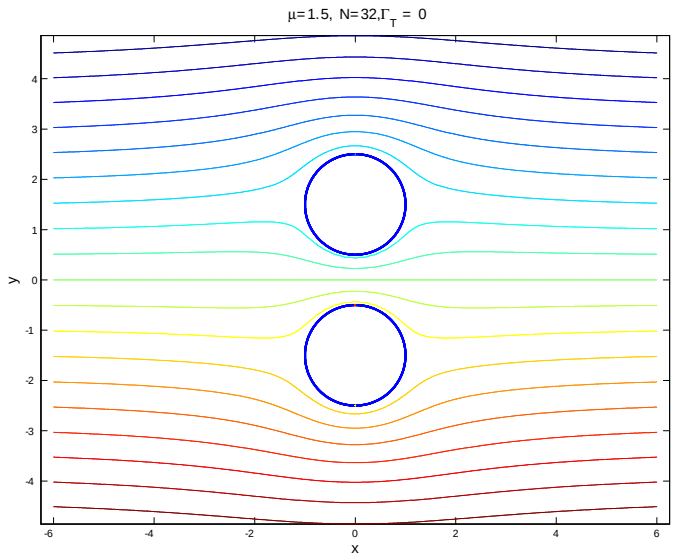

Figure 1.3: Streamlines for the initial flow. The reference frame is taken to move with the cylinders at a velocity **U**.

being, the former is the planar analogue of the latter. Computing the initially toroidal vortex sheet is in part motivated by the following. In the instance of axisymmetric vortex sheet motion, there is difficulty in evaluating the principal value equations governing the vortex sheet motion near the axis of symmetry [21]. The initially toroidal vortex sheet avoids this problem altogether; it does not intersect with its axis of symmetry.

Moore [18], Krasny [13], and Shelley [26] have shown that given analytic initial conditions, planar vortex sheets stop being analytic in finite time. At the time of singularity formation, known as the critical time, the curvature of the vortex sheets becomes infinite. There is evidence that a branch point singularity of order $\frac{3}{2}$ occurs in general for planar vortex sheets [2] [10]. This means that, with respect to the vortex sheets position, which can be parameterized by a Lagrangian parameter α, the singularity is proportional to $\alpha^{\frac{3}{2}}$. These singularities are often referred to as

Moore singularities.

Our aim is to study the evolution, singularity formation, and roll-up of the two initially cylindrical vortex sheets. The critical times, locations of singularity formations, and confirmation of the branch point singularities of order $\frac{3}{2}$, are sought. Several methodologies used by Nitsche [24] [23] are adopted here.

An overview of the methods is as follows. The continuous vortex sheets are to be discretized by a finite array of point-vortices using Rosenhead's point-vortex approximation with the addition of correction terms due to van de Vooren [28]. The sheets are then evolved under their self-induced velocities up until their finite critical times. Since the point-vortex method does not converge past the critical times [13], determining their values is of great importance to the evolutions of the vortex sheets. This is why obtaining estimates for the critical times is of interest. Parameters pertaining to the asymptotics of the Fourier coefficients of the vortex sheets' positions are then numerically fitted to gain better insight into aspects of the singularity formation. These include confirming the $\frac{3}{2}$ order of the branch-point singularities, and better determining the critical times and locations of singularity formation. Furthermore, there is indication that more than one singularity forms on each vortex sheet, and that for most cases, one singularity forms prior to the other. We seek similar information to the second singularity formation as that of the first, namely, its order, location, and time of formation. In order to do so, we implement a smoothing over initial singularity formations by either the heat equation or through a local application of the vortex blob method in lieu of the normal governing equations over that region. Note that the vortex blob method introduces an artificial parameter δ into the singular governing equations so that they can be regularized [4].[5] The vortex sheet roll-up is further studied by the use of the vortex-blob method; this method is needed to evolve the vortex sheets past their critical times. The effects

[5]This regularization parameter δ is not to be confused with the Dirac-delta function δ mentioned below.

of varying the initially prescribed total circulation around each vortex sheet on their evolutions and singularity formations will also be taken into consideration.

A brief mentioning of two main numerical tools are also in order. Firstly, the non-regularized equations governing the vortex sheet motion are principal value integrals. The accurate approximation of these integrals is due to van de Vooren [28]. Secondly, prior to the critical times, there exists a type of irregular motion in the point-vortices' positions[6], which is due to the growth of computer round off error from Kelvin-Hemholtz instability. This irregular point motion is controlled by both increasing the machine precision and through the introduction of Krasny's Fourier filter, which sets high wavenumber modes up to an appropriately specified threshold in the Fourier coefficients of the vortex sheet's positions to zero so that they cannot grow due to Kelvin-Hemholtz instability [13]. When implementing Krasny's Fourier filter, at each timestep of the vortex sheet's evolution, we apply the Fourier transform to the point-vortices' positions, set all modes below a designated threshold to zero, and then apply the inverse Fourier transform.

1.2 Some Preliminaries

A shear layer is a thin layer which separates two regions of differing velocities. An example of this can be observed in Figure 1.4. In this figure, there is a top and bottom region of uniform flow velocities, namely $\mathbf{u} = (U^+, 0, 0)$ and $\mathbf{u} = (U^-, 0, 0)$, respectively. However, the separation layer (the shaded region between the top and bottom regions in the figure) consists of a flow with velocity $\mathbf{u} = (U(y), 0, 0)$. Outside of this separation layer, the vorticity $\boldsymbol{\xi} = \boldsymbol{\nabla} \times \mathbf{u} = \mathbf{0}$. But, within this separation layer, $\boldsymbol{\xi} = -U'(y)\,\hat{\mathbf{z}}$, where $\hat{\mathbf{z}}$ is taken to be directed out of the page. If we were to let the separation layer shrink to a region of zero thickness (Figure 1.5),

[6] that are used to approximate the vortex sheet.

then we would have what is termed a vortex sheet. That is, a vortex sheet is the interface between a shear layer of zero thickness. $\boldsymbol{\xi} = \mathbf{0}$ away from a vortex sheet[7], yet $\oint_C \mathbf{u} \bullet d\mathbf{s} = \int_S \boldsymbol{\xi} \bullet \mathbf{n}\, dA \neq 0$, where C is a closed contour around a portion of the vortex sheet, S is the bounded surface contained within C, and $\mathbf{n}$ is the unit normal to S. Indeed, $\boldsymbol{\xi}$ is a δ-function on the surface of the vortex sheet. Across this interface, the tangential velocity is discontinuous. This jump in tangential velocity is known as the vortex sheet strength σ, and characterizes the vortex sheet [19]. The normal velocity component is continuous. Chorin and Marsden put it simply, "a vortex sheet is a surface (or a curve) that is tangent to the vorticity vector $\boldsymbol{\xi}$ at each of its points". Let us add that $\boldsymbol{\xi} = \mathbf{0}$ away from the surface. They also state, "If a surface (or curve) moves with the flow[8] and is a vortex sheet (or line) at $t = 0$, then it remains so for all time" [5, p. 22-23]. So for our particular vortex sheet evolution, the vortex sheet will remain such for all time.

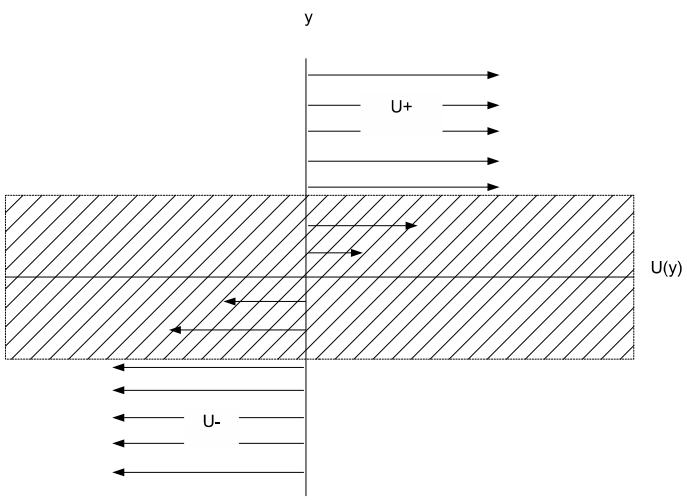

Figure 1.4: Example of a shear layer

[7]It is being assummed the flow is potential away from the vortex sheet.
[8]of an isentropic fluid. Note that irrotational flows are isentropic [3].

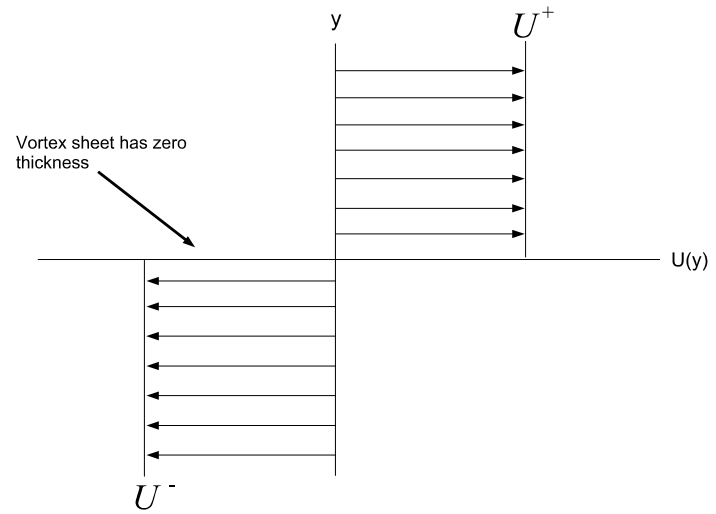

Figure 1.5: Example of a vortex sheet approximation

The location of a closed two-dimensional vortex sheet at time t is given by the curve $\mathbf{x}(\alpha, t) = \begin{pmatrix} x(\alpha, t) \\ y(\alpha, t) \end{pmatrix}$, where α denotes a Lagrangian parameter. See Figure 1.6. α is invariant in time for a specific mass of fluid on the sheet; specific values of α can be said to correspond to specific masses of fluid on the sheet, for all time. We

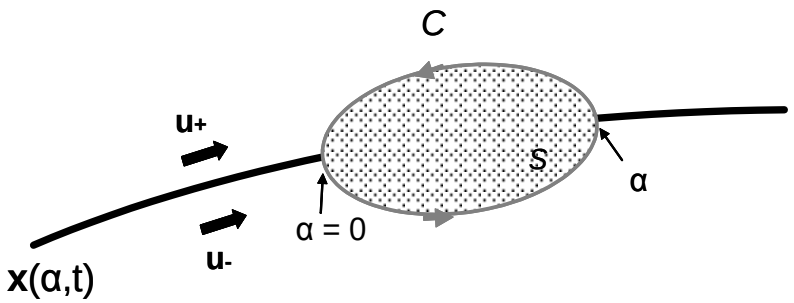

Figure 1.6: Contour C of a vortex sheet.

have $\frac{D\alpha}{Dt} \equiv \frac{\partial \alpha}{\partial t} + \mathbf{u} \cdot \nabla \alpha = 0$. We choose a particular mass of fluid on the sheet will move as described by $\mathbf{u} = \frac{\partial \mathbf{x}(\alpha,t)}{\partial t} = \frac{1}{2}(\mathbf{u}_+ + \mathbf{u}_-)$, where $\mathbf{u}_+$ and $\mathbf{u}_-$ are the respective velocity fields outside and inside the vortex sheet [19] It is the normal component of $\mathbf{u}$ to the boundary of the vortex sheet that will determine how the vortex sheet moves. The tangential component of $\mathbf{u}$ to the boundary of the vortex sheet will determine how the individual particles move on the sheet.

Consider a closed counterclockwise contour C of fluid that contains a part of the vortex sheet within it, and let C_t be the contour carried by the flow. The circulation around C_t is given by $\Gamma_{C_t} = \oint_{C_t} \mathbf{u} \bullet d\mathbf{s}$. Γ_{C_t} is constant in time according to Kelvin's Circulation Theorem [5].[9] Also, via Stokes' theorem $\Gamma_C = \int_D (\nabla \times \mathbf{u}) \bullet \mathbf{n}\, ds = \int_D \boldsymbol{\xi} \bullet \mathbf{n}\, ds$, where D is the region bounded by C. Let us now consider a small portion of vortex sheet with arclength Δs. Then the circulation around a small rectangular contour C enclosing only this portion of the vortex sheet is given by $\Delta\Gamma = \oint_C \mathbf{u} \bullet d\mathbf{s} \approx -u_+ \Delta s + u_- \Delta s = -[u_+ - u_-]\Delta s$, where u_+ and u_- are the corresponding limiting tangential velocity components above and below the vortex sheet. So $\sigma(s) = \frac{d\Gamma}{ds} \approx \frac{\Delta\Gamma}{\Delta s} \approx -[u_+ - u_-]$. Define the circulation distribution around the vortex sheet from a fixed point on the sheet, corresponding to $\alpha = 0$, to an arbitrary point α to be $\Gamma(\alpha) = \int_0^{s(\alpha)} \sigma(s)\ ds$, where $s(\alpha)$ is the arclength from the fixed point to the arbitrary point.

1.3 Paper Organization

This paper is organized as follows. Chapter 2 describes the problem formulation, initial conditions, and evolution equations. Chapter 3 describes the numerical methods used in the evolution of the vortex sheets, including integral approximations, effects

[9] This holds for isentropic flow without external forces. Also, there is the issue that the contour intersecting the vortex sheet doesn't remain closed (resulting from the discontinuous velocity across the sheet), which is addressed in [28].

of computer precision, and Krasny's Fourier filter. Chapter 4 presents the numerical results for the sheets' evolution, and certain estimates regarding singularity formation. Chapter 5 pertains to further aspects of the singularity formation; including a description and least-squares fittings of parameters contained in the asymptotic form of the Fourier coefficients corresponding to the vortex sheet's positions, and smoothings over initial singularity formations. Chapter 6 includes simulations past the time of singularity formation with the implementation of the vortex blob method, and includes some of the effects of varying the initially prescribed total circulation around the vortex sheets. Chapter 7 serves as a conclusion to the paper.

Chapter 2

Problem Formulation

2.1 Initial Conditions

Consider two identical cylindrical vortex sheets whose axes are parallel to the z-axis, and have radii R. Let their centers fall on the y-axis and each be a distance $D > R$ from the x-axis; with one sheet above and one sheet below the x-axis. Suppose their z-directed lengths are very large. Due to symmetry, at time t, the two vortex sheets are described by the cross section of the top cylindrical sheet with the x-y plane via $\mathbf{x}(\alpha, t) = \begin{pmatrix} x(\alpha, t) \\ y(\alpha, t) \end{pmatrix}$ and $\Gamma(\alpha)$, where α is a Lagrangian parameter. Initially, this curve is given by

$$\mathbf{x}(\alpha, 0) = \begin{pmatrix} x(\alpha, 0) \\ y(\alpha, 0) \end{pmatrix} = \begin{pmatrix} R\cos\alpha \\ D + R\sin\alpha \end{pmatrix}, \text{ where } \alpha \in [0, 2\pi]. \tag{2.1}$$

The curve is 2π-periodic with respect to α. Figure 2.1 gives a schematic of this setup. Since $D > R$; the two vortex sheets will then not initially touch each other. Due to symmetry, the cross section curve of the bottom cylindrical sheet in the x-y plane is easily deduced. Moreover, due to the given symmetry of the vortex sheets, when

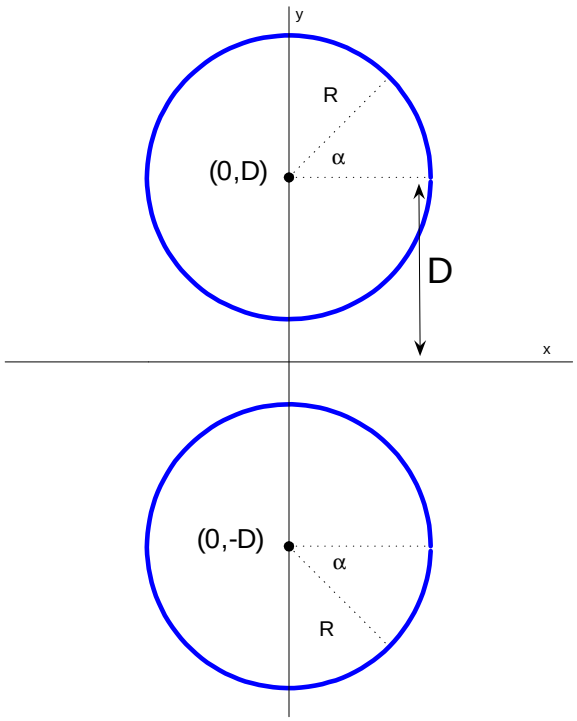

Figure 2.1: Cross section of the initial vortex sheets in the x-y plane.

the two sheets are evolved in time, the shape of the top sheet will dictate the shape of the bottom sheet. As such, we need only consider the behavior of the top sheet. We prescribe the vortex sheets and the fluid contained within the vortex sheets to have an initial velocity given by $\mathbf{U} = (U, 0, 0)$.[1][2] The flow is non-dimensionalized[3]

[1]This reference frame is chosen in part so as to be consistent with that of [24].

[2]One could make a change in reference frames so that the initial velocity inside the vortex sheets is set to $\mathbf{U} = (0, 0, 0)$. The velocity field outside the vortex sheets would then need to be changed by subtracting U from the previously $\hat{\mathbf{x}}$ directed velocity field component for outside the vortex sheets. In that case, the flow far away from the vortex sheets would become a uniform rectilinear flow described by the velocity field $(-U, 0, 0)$. And initially, the flow would then be analogous to a $-\hat{\mathbf{x}}$ directed uniform rectilinear flow of magnitude U past two solid cylinders.

[3]The details of the non-dimensionalization are given in Appendix A.

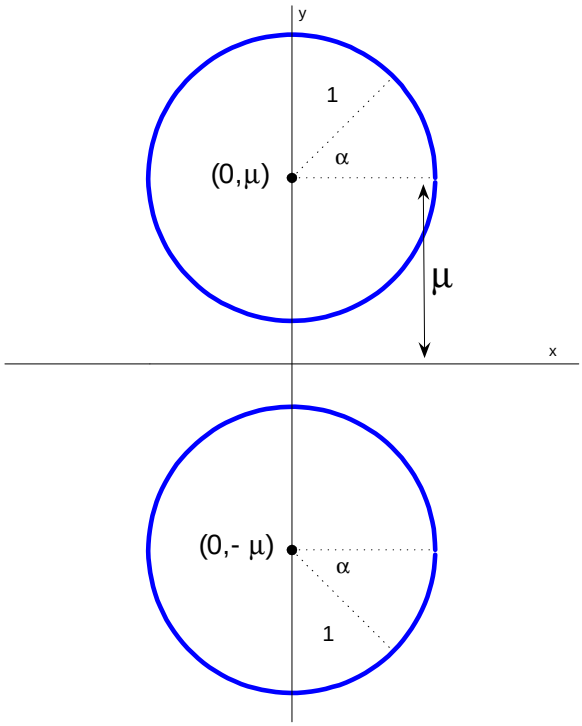

Figure 2.2: Cross section of the initial non-dimensionalized vortex sheets in the x-y plane.

so that the cross section of the top vortex in the x-y plane sheet is then initially described according to

$$\mathbf{x}(\alpha, 0) = \begin{pmatrix} \cos\alpha \\ \mu + \sin\alpha \end{pmatrix}, \text{ where } \mu \equiv \frac{D}{R} > 1. \tag{2.2}$$

Figure 2.2 shows these non-dimensionalized changes. The non-dimensionalized initial velocity for the vortex sheets and the fluid contained within the vortex sheets is $\mathbf{U} = (1, 0, 0)$.[4] As described in Section 1.1, the initial boundary condition upon the

[4]This reference frame is chosen in part so as to be consistent with that of [24].

vortex sheets are given by $\mathbf{u} \cdot \mathbf{n} = \mathbf{U} \cdot \mathbf{n}$. The arclength is given by $s = R\alpha$. The total circulation (distribution) around each entire vortex sheet

$$\Gamma_{\mathrm{T}} = \Gamma(2\pi) = \int_0^{s(2\pi)} \sigma(s)\ ds \tag{2.3}$$

needs to also be initially set.[5] With these constraints, the initial velocity field of the flow outside the vortex sheets can be determined.

2.2 Evolution Equations

Two-dimensional vortex sheet evolution at the point $\mathbf{x}(\alpha, t) = \begin{pmatrix} x(\alpha,t) \\ y(\alpha,t) \end{pmatrix}$ is governed by the velocity equations

$$\mathbf{u}(\mathbf{x}, t) = \frac{1}{2\pi} P.V. \int_C \frac{1}{(x-\tilde{x})^2 + (y-\tilde{y})^2} \begin{pmatrix} \tilde{y}-y \\ x-\tilde{x} \end{pmatrix} \Gamma'(\tilde{\alpha})\ d\tilde{\alpha}, \tag{2.4}$$

where C is the counterclockwise contour along the entire vortex sheet, $\tilde{\mathbf{x}}(\alpha, t)$ denotes the vortex sheet positions inducing the motion, and $\Gamma(\tilde{\alpha})$ is the circulation distribution. Thus, if one gives the initial position of a vortex sheet, and can solve for $\Gamma'(\tilde{\alpha})$, the motion is determined. (2.4) is known as the Birkhoff-Rott equation.

For our particular problem of the two initially cylindrical vortex sheets, (2.4) becomes

$$\begin{aligned} \mathbf{u}(\mathbf{x}, t) \;=\; & \frac{1}{2\pi} P.V. \int_0^{2\pi} \frac{1}{(x-\tilde{x})^2 + (y-\tilde{y})^2} \begin{pmatrix} \tilde{y}-y \\ x-\tilde{x} \end{pmatrix} \Gamma'(\tilde{\alpha})\ d\alpha \\ & + \frac{1}{2\pi} \int_0^{2\pi} \frac{1}{(x-\tilde{x})^2 + (y+\tilde{y})^2} \begin{pmatrix} y+\tilde{y} \\ \tilde{x}-x \end{pmatrix} \Gamma'(\tilde{\alpha})\ d\alpha. \end{aligned} \tag{2.5}$$

[5] Γ_{T} will remain constant throughout all time.

Recall that the vortex sheets in our problem are symmetric about the x-axis, and the induced velocities from both sheets needs to be taken into account. The initial vortex sheets' positions are given by (2.2). With a total prescribed circulation Γ_T around each vortex sheet, and use of the boundary condition $\mathbf{u} \cdot \mathbf{n} = \mathbf{U} \cdot \mathbf{n}$, we will find $\Gamma'(\tilde{\alpha})$.[6] If this can be done, the motion for our problem can be determined. Equations (2.5) fail to converge past the time of singularity formation in the vortex sheets' positions.

One approach to describe the motion of the vortex sheets past these times of singularity formation is to regularize equation (2.5) by the introduction of an artificial parameter δ. This method is known as the vortex blob method [23] [4] [14]. It gives the velocity at $\mathbf{x}$ by

$$\begin{aligned} \mathbf{u}(\mathbf{x},t) &= \frac{1}{2\pi}\int_0^{2\pi} \frac{1}{(x-\tilde{x})^2+(y-\tilde{y})^2+\delta^2} \begin{pmatrix} \tilde{y}-y \\ x-\tilde{x} \end{pmatrix} \Gamma'(\tilde{\alpha})\ d\alpha \\ &\quad + \frac{1}{2\pi}\int_0^{2\pi} \frac{1}{(x-\tilde{x})^2+(y+\tilde{y})^2+\delta^2} \begin{pmatrix} y+\tilde{y} \\ \tilde{x}-x \end{pmatrix} \Gamma'(\tilde{\alpha})\ d\alpha. \end{aligned} \tag{2.6}$$

In the limit $\delta \to 0$, it is known that the solution to (2.6) converges to the solution for that of (2.5) prior to singularity formation.

2.2.1 Finite Array of Point Vortices

Equations (2.4) can be constructed by considering the following:

Suppose an incompressible, almost potential flow where the vorticity is concentrated at a finite array of N point-vortices located in a plane at positions $\mathbf{x}_k$, with respective circulations $\Delta\Gamma_k$, where $k = 1, 2, ..., N$. At each of these point-vortices

[6] Note that at time $t = 0$, the vortex sheet strength $\sigma(\tilde{s}) = \Gamma'(\tilde{\alpha})$.

the vorticity field is singular. Away from the point vortices, the flow is potential. Now, the stream function at location $\mathbf{x} = \begin{pmatrix} x \\ y \end{pmatrix}$ due to an individual point-vortex located at position $\mathbf{x}_k$ is given by

$$\psi_k(\mathbf{x}) = -\frac{\Delta\Gamma_k}{2\pi} \log \|\mathbf{x} - \mathbf{x}_k\| . \tag{2.7}$$

The contribution to the velocity field solely from the point-vortex at position $\mathbf{x}_k$ is given by

$$\mathbf{u}_k(\mathbf{x}) = \begin{pmatrix} \frac{\psi_k(\mathbf{x})}{\partial y} \\ -\frac{\psi_k(\mathbf{x})}{\partial x} \end{pmatrix} = \frac{\Delta\Gamma_k}{2\pi} \frac{1}{(x - x_k)^2 + (y - y_k)^2} \begin{pmatrix} y_k - y \\ x - x_k \end{pmatrix} \tag{2.8}$$

Via superposition, the stream function resulting from the entire array of point-vortices is given by $\psi(\mathbf{x}) = \sum_{k=1}^{N} \psi_k(\mathbf{x})$. And, the total induced velocity field becomes

$$\mathbf{u}(\mathbf{x}, t) = \sum_{\substack{k=1 \\ \mathbf{x} \neq \mathbf{x}_k}}^{N} \mathbf{u}_k(\mathbf{x}, t) = \frac{1}{2\pi} \sum_{\substack{k=1 \\ \mathbf{x} \neq \mathbf{x}_k}}^{N} \frac{\Delta\Gamma_k}{(x - x_k)^2 + (y - y_k)^2} \begin{pmatrix} y_k - y \\ x - x_k \end{pmatrix} \tag{2.9}$$

Thus, a point-vortex located at $\mathbf{x}_j$ will move as described by[7]

$$\mathbf{u}(\mathbf{x}_j, t) = \begin{pmatrix} \frac{dx_j}{dt} \\ \frac{dy_j}{dt} \end{pmatrix} = \frac{1}{2\pi} \sum_{\substack{k=1 \\ k \neq j}}^{N} \frac{\Delta\Gamma_k}{(x_k - x_j)^2 + (y_k - y_j)^2} \begin{pmatrix} y_k - y_j \\ x_j - x_k \end{pmatrix} . \tag{2.10}$$

The point-vortices evolve under self-induced motion. The positions $\mathbf{x}_k$ and respective circulations $\Delta\Gamma_k$, $k = 1, 2, ..., N$, of the point-vortices will need to be prescribed. Not only will the circulations $\Delta\Gamma_k$ at each point-vortex remain constant throughout time; but also will the total circulation distribution $\Gamma_T = \sum_{k=1}^{N} \Delta\Gamma_k$ [5].

By letting $N \to \infty$ and $\Delta\Gamma \to 0$ in (2.10), we then get (2.4).

[7]The constraint $k \neq j$ in the summation is made so that the self-induced contribution of the point-vortex to the velocity field is not included.

2.2.2 Point-Vortex Approximation Applied to the Two Cylindrical Vortex Sheets

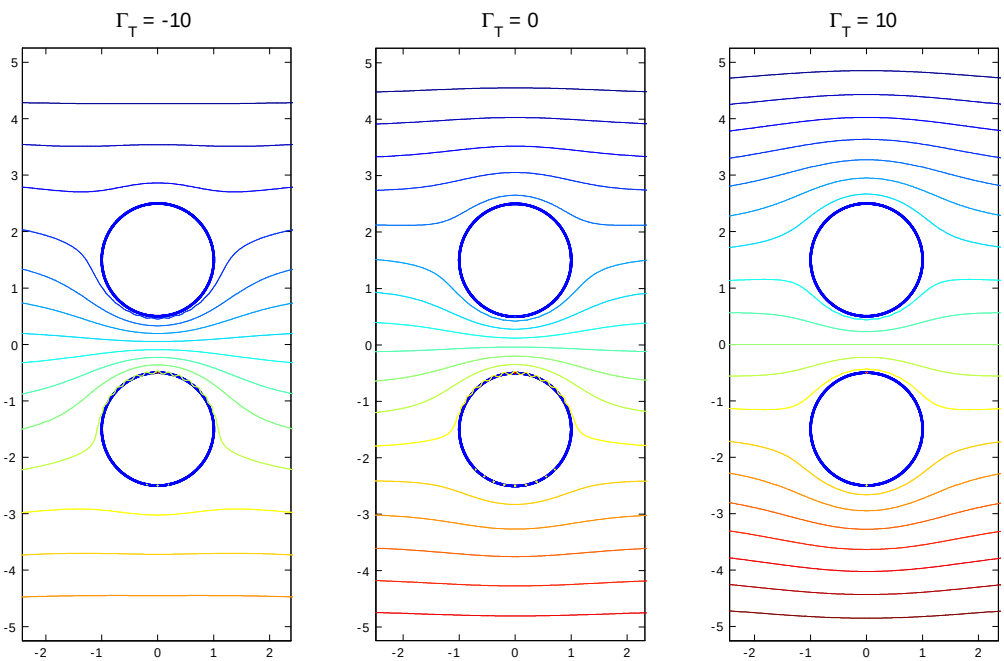

Figure 2.3: Streamlines for the initial flow past the cylindrical, counter-rotating vortex sheets, with $\Gamma_T = -10,\ 0,\ 10$. For these plots, $\mu = 1.5$ and $N = 32$.

Consider the cylindrical vortex sheets described in Section 2.1. Replace each vortex sheet by an array of N point-vortices uniformly spaced throughout the entire sheet, which are located at $\mathbf{x}_k = \mathbf{x}(\alpha_k, t)$, corresponding to the uniform mesh given by $\alpha_k = (k-1)\,\Delta\alpha$, where $\Delta\alpha = \frac{2\pi}{N}$, and with respective circulations $\Delta\Gamma_k$, where $k = 1, 2, ..., N$. This approximation of the vortex sheet is known as Rosenhead's point-vortex approximation. At a position $\mathbf{x}$, the stream function due to the contributions from the two arrays each consisting of N point-vortices used in approximating the

two cylindrical vortex sheets is given by

$$\begin{aligned}\psi(\mathbf{x}) &= -\frac{1}{2\pi}\sum_{k=1}^{N}\Delta\Gamma_k \log\sqrt{(x-x_k)^2+(y-y_k)^2} \\ &\quad -\frac{1}{2\pi}\sum_{k=1}^{N}\Delta\Gamma_k^B \log\sqrt{(x-x_k^B)^2+(y-y_k^B)^2}.\end{aligned} \tag{2.11}$$

$\left(x_k^B, y_k^B\right)$ and $\Delta\Gamma_k^B$, $k = 1, 2, .., N$, denote the locations of the point-vortices and corresponding circulations on the bottom vortex sheet. These locations and circulations are related to those on the top vortex sheet via $\left(x_k^B, y_k^B\right) = (x_k, -y_k)$ and $\Delta\Gamma_k^B = -\Delta\Gamma_k$. Thus the stream function due to the two arrays of point-vortices can be written as

$$\psi(\mathbf{x}) = \frac{1}{2\pi}\sum_{k=1}^{N}\Delta\Gamma_k\left[-\log\sqrt{(x-x_k)^2+(y-y_k)^2}+\log\sqrt{(x-x_k)^2+(y+y_k)^2}\right]. \tag{2.12}$$

The total induced velocity field would then become

$$\begin{aligned}\mathbf{u}(\mathbf{x},t) &= \begin{pmatrix}\frac{\psi_k(\mathbf{x})}{\partial y}\\ \frac{\psi(\mathbf{x})}{\partial x}\end{pmatrix} = \frac{1}{2\pi}\sum_{\substack{k=1\\k\neq j}}^{N}\frac{\Delta\Gamma_k}{(x-x_k)^2+(y-y_k)^2}\begin{pmatrix}y_k-y\\ x-x_k\end{pmatrix} \\ &\quad +\frac{1}{2\pi}\sum_{k=1}^{N}\frac{\Delta\Gamma_k}{(x-x_k)^2+(y+y_k)^2}\begin{pmatrix}y+y_k\\ x_k-x\end{pmatrix}.\end{aligned} \tag{2.13}$$

Thus, a point-vortex located at $\mathbf{x}_j$ will move as described by

$$\begin{aligned}\mathbf{u}(\mathbf{x}_j,t) &= \frac{1}{2\pi}\sum_{\substack{k=1\\k\neq j}}^{N}\frac{\Delta\Gamma_k}{(x_j-x_k)^2+(y_j-y_k)^2}\begin{pmatrix}y_k-y_j\\ x_j-x_k\end{pmatrix} \\ &\quad +\frac{1}{2\pi}\sum_{k=1}^{N}\frac{\Delta\Gamma_k}{(x_j-x_k)^2+(y_j+y_k)^2}\begin{pmatrix}y_j+y_k\\ x_k-x_j\end{pmatrix}.\end{aligned} \tag{2.14}$$

By letting $N \to \infty$ and $\Delta\Gamma \to 0$ in (2.14), we then get (2.5).

Figure 2.3 shows the streamlines, or level curves, of ψ with the prescribed nondimensionalized uniform flow $\mathbf{U} = (1, 0, 0)$, for $\Gamma_T = -10$, 0, and 10. They were constructed using 2.12. In these plots, $\mu = 1.5$ and $N = 32$. Observe that especially for $\Gamma_T = -10$ and $\Gamma_T = 0$, the streamlines are more dense in the region between the two cylinders than for the regions above and below the two cylinders. Thus, according the Bernoulli's theorem[8], there is a smaller pressure distribution in the region between the two spheres [25, p. 109]. This pressure differential causes the cylinders to move together. As Γ_T is increased, this pressure differential will decrease; eventually, another pressure differential will take effect and the two cylinders will be pushed apart. Additionally, the y-axis symmetry of the streamlines implies that there is no drag on the initial sheets [5]. The stagnation points, defined where the pressure is a greatest, will lie on the boundaries of the cylinders for $|\Gamma_T|$ sufficiently small. As $|\Gamma_T|$ increases, the location of the stagnation points will move off of the boundaries of the cylinders and into the flow [8].

It is permissible to replace the array of point vortices[9] in this figure with a solid cylinder in which the point vortices' locations would lie on the boundary of the cylinder; the flow outside the array of point vortices would remain unchanged. If we were to only consider the case of flow past one cylinder (i.e. the limiting case $\mu \to \infty$ in our problem), the cylinder could be replaced with a doublet of suitable strength having the same center as of the cylinder, and again the flow outside the radius of the cylinder would remain unchanged [11]. For this appropriately placed doublet of suitable strength, there would be a circular streamline that is the same position as that of the cylinder. In addition, on any streamline $\psi(\mathbf{x}) =$ constant,

[8]Recall that Bernoulli's theorem states that $p = H - \frac{1}{2}|\mathbf{u}|^2$, where p is the pressure distribution, and H is Bernoulli's constant [5] [8].

[9]To be more precise, this would be the case for the limiting case $N \to \infty$, where N is the number of point vortices on each vortex sheet.

the curve can be thought of as a solid boundary of the fluid [17]. In our problem, due to symmetry, a streamline actually falls upon the x-axis. An example of this can be seen in the given plot of the streamlines for $\Gamma_T = 10$. This implies that an infinite wall could be placed along the x-axis without changing the considered flow. Thus, our problem is analogous to the problem of evolving either the top or bottom rotating, initially cylindrical vortex sheet with an infinitely long wall placed on the x-axis.

2.2.3 Solving for the Initial Sheet Strength

In (2.14), by choosing uniform spacing and circulations of the point-vortices used in the vortex sheet approximations, we then have $\Delta\Gamma_k = \sigma_k \Delta s_k = \frac{2\pi}{N}\sigma_k$, where $\Delta s_k = \frac{2\pi}{N}$. If we take the discretized top vortex sheet's point-vortices to be located at positions $\mathbf{x}_j$, $j = 1, 2, ..., N$, then the normal to the discretized sheet at those points is given by $\mathbf{n}(\mathbf{x}_j) = (\cos\alpha_j, \sin\alpha_j)$, and the velocities there given by $\mathbf{u}(\mathbf{x}_j)$. Then the imposed boundary condition $\mathbf{u}\cdot\mathbf{n} = \mathbf{U}\cdot\mathbf{n}$ can be written as

$$\frac{dx_j}{dt}\cos\alpha_j + \frac{dy_j}{dt}\sin\alpha_j = \mathbf{u}(\mathbf{x}_j)\cdot\mathbf{n}(\mathbf{x}_j) = \mathbf{U}\cdot\mathbf{n}(\mathbf{x}_j) = \cos\alpha_j, \tag{2.15}$$

where $\mathbf{u}(\mathbf{x}_j) = \begin{pmatrix} \frac{dx_j}{dt} \\ \frac{dy_j}{dt} \end{pmatrix}$ is given by (2.14). Recall that the nondimensionalized $\mathbf{U}$ is given by $\mathbf{U} = (1, 0, 0)$.

Define

$$\begin{aligned} A_{\substack{jk \\ k\neq j}} &= \frac{1}{N}\left[\left(\frac{y_k - y_j}{(x_j - x_k)^2 + (y_j - y_k)^2} + \frac{y_j + y_k}{(x_j - x_k)^2 + (y_j + y_k)^2}\right)\cos\alpha_j, \right. \qquad (2.16) \\ A_{jj} &= \frac{1}{N}\left[\left(\frac{y_j + y_j}{(x_j - x_k)^2 + (y_j + y_k)^2}\right)\cos\alpha_j + \left(-\frac{x_j - x_j}{(x_j - x_j)^2 + (y_j + y_j)^2}\right)\sin\alpha_j\right]. \end{aligned}$$

Then (2.15) can be written as

$$\begin{bmatrix} A_{j1} & A_{j2} & ... & A_{jN} \end{bmatrix} \begin{bmatrix} \sigma_1 \\ \sigma_2 \\ \vdots \\ \sigma_N \end{bmatrix} = \begin{bmatrix} \cos\alpha_j \end{bmatrix}. \tag{2.17}$$

This is equivalent to the system $A\boldsymbol{\sigma} = \mathbf{b}$, where $A = \begin{bmatrix} A_{11} & ... & A_{1N} \\ A_{21} & ... & A_{2N} \\ \vdots & \ddots & \vdots \\ A_{N1} & ... & A_{NN} \end{bmatrix}$, $\boldsymbol{\sigma} = \begin{bmatrix} \sigma_1 \\ \sigma_2 \\ \vdots \\ \sigma_N \end{bmatrix}$, and $\mathbf{b} = \begin{bmatrix} \cos\alpha_1 \\ \cos\alpha_2 \\ \vdots \\ \cos\alpha_N \end{bmatrix}$. Initially, A and $\mathbf{b}$ are known.[10] So we can solve for the initial sheet strength $\boldsymbol{\sigma}$.

When we proceed to solve this system in Matlab via the command $\boldsymbol{\sigma} = A\backslash\mathbf{b}$, we get the results as presented in Figure 2.4. Convergence in $\boldsymbol{\sigma}$ is not observed as N is increased. In addition, condition number of A is very large (Figure 2.5), and thus, A is poorly conditioned. Matlab gives the following error: *Matrix is close to singular or badly scaled. Results may be inaccurate.* These poor results are expected, as the total circulation Γ_{T} around each vortex sheet has not yet been prescribed.

Let us now define

$$\mathbf{x}_j^m = \left(x_j^m, y_j^m\right) = \left(\cos\alpha_j^m, \mu + \sin\alpha_j^m\right), \text{ where } \alpha_j^m = \alpha_j + \frac{\pi}{N}. \tag{2.18}$$

$\mathbf{x}_j^m$ be located on the approximated vortex sheet half-way, that is at the "midpoint", between the two neighboring point-vortices. Let us approximate the velocities at

[10] Note that we have N unknowns in $\boldsymbol{\sigma}$; and N equations in $A\boldsymbol{\sigma} = \mathbf{b}$.

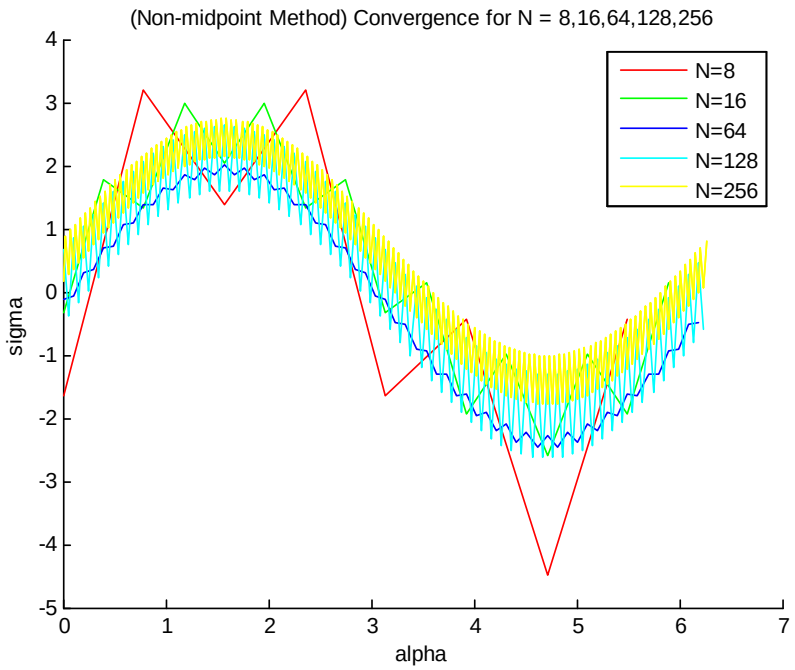

Figure 2.4: Computed initial sheet strengh σ vs. α using the non-midpoint method.

$\mathbf{u}(\mathbf{x}_j)$ by actually evaluating them at $\mathbf{x}_j^m$ instead of at $\mathbf{x}_j$. That is, for evaluation purposes we are making[11]

$$\begin{aligned}\mathbf{u}\left(\mathbf{x}_j^m\right) &= \frac{1}{2\pi}\sum_{k=1}^{N}\frac{\Delta\Gamma_k}{\left(x_j^m-x_k\right)^2+\left(y_j^m-y_k\right)^2}\begin{pmatrix}y_k-y_j^m\\ x_j^m-x_k\end{pmatrix}\\ &\quad+\frac{1}{2\pi}\sum_{k=1}^{N}\frac{\Delta\Gamma_k}{\left(x_j^m-x_k\right)^2+\left(y_j^m+y_k\right)^2}\begin{pmatrix}y_j^m+y_k\\ x_k-x_j^m\end{pmatrix}.\end{aligned} \tag{2.19}$$

We impose (2.15), but now with evaluating $\mathbf{n}$ at $\mathbf{x}_j^m$ in lieu of $\mathbf{x}_j$, and approximating $\mathbf{u}(\mathbf{x}_j)$ with $\mathbf{u}\left(\mathbf{x}_j^m\right)$ as given in (2.19). We now re-define A and $\mathbf{b}$ according to

[11] The $k \neq j$ constraint in the first summation of the velocity field is now lifted.

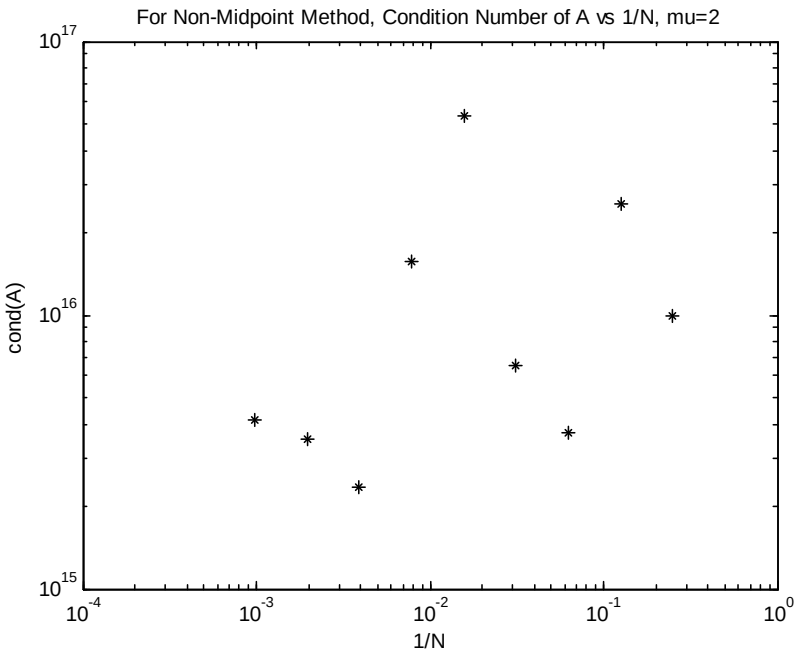

Figure 2.5: cond(A) vs. $\frac{1}{N}$ for non-midpoint method.

$$\begin{aligned} A_{jk} &= \frac{1}{N}\Bigg[\left(\frac{y_k - y_j^m}{\left(x_j^m - x_k\right)^2 + \left(y_j^m - y_k\right)^2} + \frac{y_j^m + y_k}{\left(x_j^m - x_k\right)^2 + \left(y_j^m + y_k\right)^2}\right)\cos\alpha_j^m \\ &\quad + \left(\frac{x_j^m - x_k}{\left(x_j^m - x_k\right)^2 + \left(y_j^m - y_k\right)^2}\,\frac{x_k - x_j^m}{\left(x_j^m - x_k\right)^2 + \left(y_j^m + y_k\right)^2}\right)\sin\alpha_j^m\Bigg], \\ \text{where } b_j &= \cos\alpha_j^m. \end{aligned} \tag{2.20}$$

With the newly defined terms, we again have a slightly different system $A\boldsymbol{\sigma} = \mathbf{b}$. We refer to this methodology as the midpoint method.

In this instance, A has a slightly better condition number (Figure 2.7) than before, but is still poorly conditioned. Matlab still yields the error: *Matrix is close to singular or badly scaled. Results may be inaccurate.* Even though there is still

not convergence of the $\boldsymbol{\sigma}$'s as N is increased (Figure 2.6), there is less oscillatory behavior than that in Figure 2.4. These poor results are again expected, as the total circulation Γ_{T} around each vortex sheet still has not been taken into account.

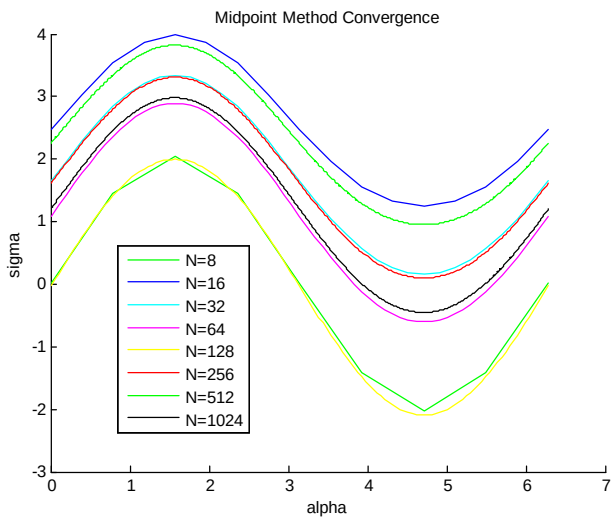

Figure 2.6: Computed initial sheet strengh σ vs. α using the midpoint method.

Let us now take into account the total initial circulation Γ_{T} around each vortex sheet. We have

$$\begin{aligned} \Gamma_{\mathrm{T}} &= \sum_{k=1}^{N} \Delta\Gamma_k = \sum_{k=1}^{N} \sigma_k \Delta s_k = \frac{2\pi}{N} \sum_{k=1}^{N} \sigma_k, \qquad (2.21) \\ \text{where } \Delta s_k &= \Delta s = \frac{2\pi}{N}. \end{aligned}$$

For $j = 1, 2, ..., N$ and $k = 1, 2, ..., N$, let us use A_{jk} and b_j as defined by (2.20) in the midpoint method. For $j = N + 1$ and $k = 1, 2, ..., N$, define $A_{jk} = \Delta s = \frac{2\pi}{N}$ and

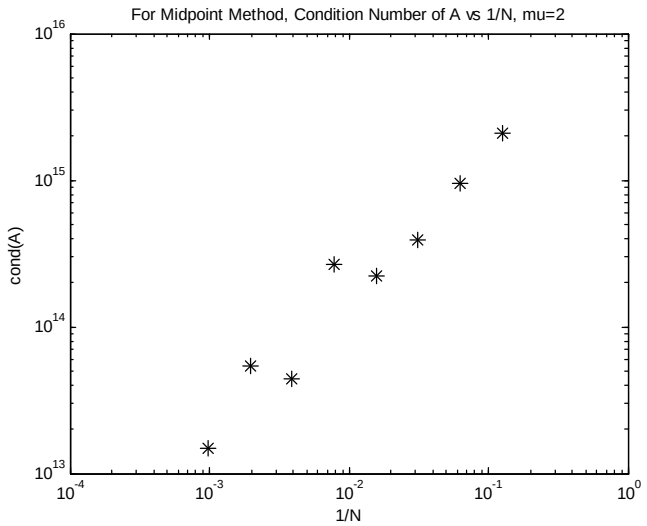

Figure 2.7: cond(A) vs. $\frac{1}{N}$ for midpoint method.

$b_j = \Gamma_{\mathrm{T}}$. This corresponding system can be written as

$$\begin{bmatrix} A_{11} & \dots & A_{1N} \\ A_{21} & \dots & A_{2N} \\ \vdots & \ddots & \vdots \\ A_{N1} & \dots & A_{NN} \\ \frac{2\pi}{N} & \dots & \frac{2\pi}{N} \end{bmatrix} \begin{bmatrix} \sigma_1 \\ \sigma_2 \\ \vdots \\ \sigma_N \end{bmatrix} = \begin{bmatrix} \cos\alpha_1 \\ \cos\alpha_2 \\ \vdots \\ \cos\alpha_N \\ \Gamma_{\mathrm{T}} \end{bmatrix} \tag{2.22}$$

or again, $A\boldsymbol{\sigma} = \mathbf{b}$. This system is now overdetermined[12] however, and is to be solved in the least squares sense. $\boldsymbol{\sigma}$ was originally computed in Matlab again using the command $\boldsymbol{\sigma} = A\backslash\mathbf{b}$ for the preliminary results. These results for $\Gamma_{\mathrm{T}} = 0$ are shown in Figure 2.8. Convergence of $\boldsymbol{\sigma}$ as N is increased is now observed. And, A now has a significantly better condition number than before (Figure 2.9). The maximum relative error in $\boldsymbol{\sigma}$ given by $\max\left|\frac{\boldsymbol{\sigma}_{\mathrm{exact}} - \boldsymbol{\sigma}_{\mathrm{N}}}{\boldsymbol{\sigma}_{\mathrm{exact}}}\right|$ versus N, where $\boldsymbol{\sigma}_{\mathrm{N}}$ corresponds to the σ used in the point-vortex approximation with N point-vortices on each sheet, and σ_{exact} is supposed to be $\boldsymbol{\sigma}_{1024}$, is shown in Figure 2.10.

[12]Note that we now have N unknowns in $\boldsymbol{\sigma}$; and $N+1$ equations in $A\boldsymbol{\sigma} = \mathbf{b}$.

Note that in computations performed later in this work, $\boldsymbol{\sigma}$ was computed in Fortran. The subroutine HFTI, which was downloaded from the netlib repository [20], was used to solve the overdetermined system by Householder transformations.[13]

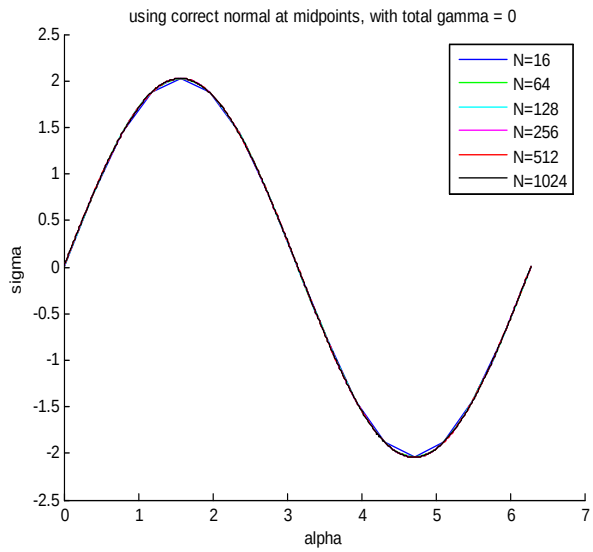

Figure 2.8: $\boldsymbol{\sigma}$ vs α, with the implemented constraint $\Gamma_T = 0$.

The plot of σ vs. α for several values of μ with $\Gamma_{\mathrm{T}} = 0$ is given in Figure 2.11. As μ approaches 1, $\boldsymbol{\sigma}$ becomes significantly more negative in the neighborhood about $\alpha = \frac{3\pi}{2}$. As μ increases, $\sigma(\alpha)$ approaches $2\sin\alpha$, indicated by the dashed line in Figure 2.11. This is consistent with $\sigma(\alpha) = 2U\sin\theta$ (where we have $U = 1$) given in limiting case of one cylindrical vortex sheet, as studied in [24]. Comparing $\sigma(\alpha)$ to each other for different values of μ can be used to roughly see how much the sheets' evolutions will be similar to each other. Note that for large μ (i.e. $\mu > 5$), the values of $\sigma(\alpha)$ are very close to each other; indicating that for large μ values, we expect further initial prescribed separation between the sheets as indicated by μ to result in fairly insignificant changes to the sheets' evolutions.

[13]Unless otherwise indicated, it is assumed that $\Gamma_{\mathrm{T}} = 0$, even though other values of Γ_{T} are just as permissible.

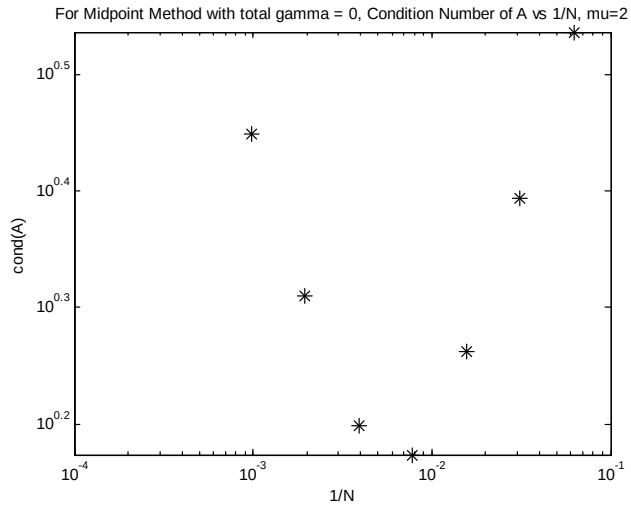

Figure 2.9: cond(A) vs. $\frac{1}{N}$, with the implemented constraint $\Gamma_T = 0$.

Different prescribed values of the total circulation constraint Γ_{T} change the respective values of $\sigma\,(\alpha)$. Larger values of Γ_{T} will impart larger values of $\sigma\,(\alpha)$. This

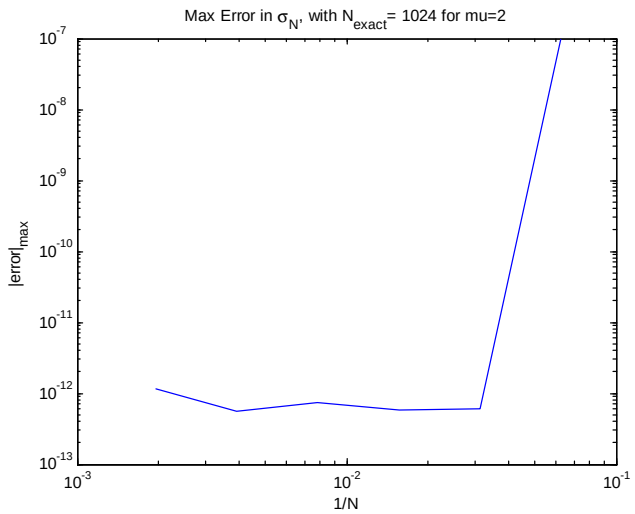

Figure 2.10: max $\left|\frac{\sigma_{\mathrm{exact}}-\sigma_{\mathrm{N}}}{\sigma_{\mathrm{exact}}}\right|$ vs. N, with the implemented constraint $\Gamma_T = 0$.

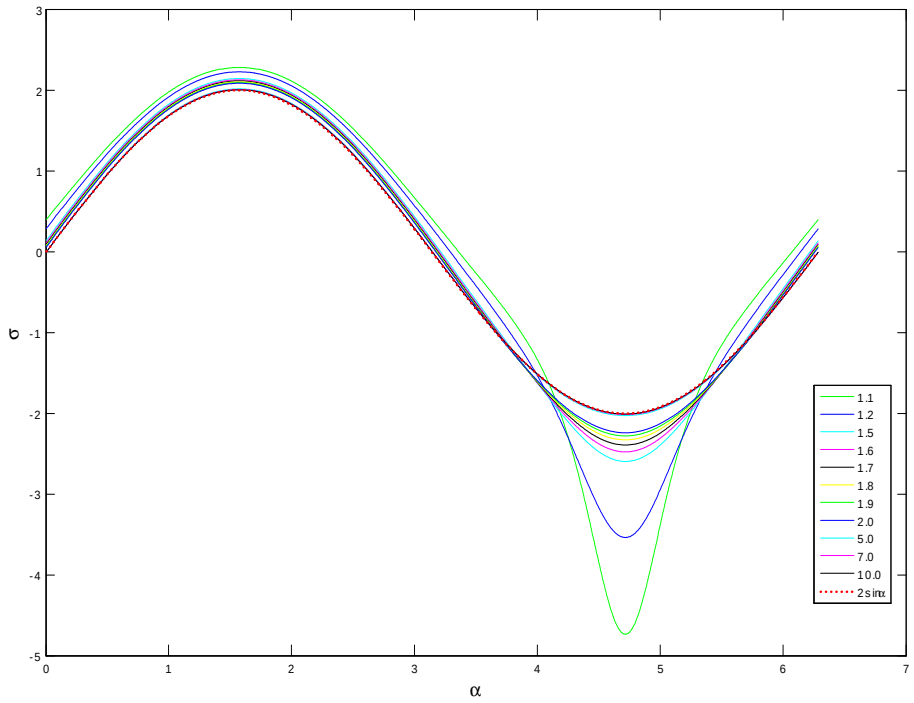

Figure 2.11: σ vs. α for different values of μ listed in the legend, with $N = 2048$ and $\Gamma_{\mathrm{T}} = 0$. The larger values of μ correspond to the larger values of $\sigma(\alpha)$. The dashed line is the plot of $2\sin\alpha$.

can be seen in Figure 2.12.

Since the analytical solutions for uniform potential flow past two (and multiple) cylinders with and without circulation can be found [7] [8] [9], it would be possible to compare our results of $\sigma(\alpha)$ with the $\sigma(\alpha)$ given by the mentioned analytical solutions.

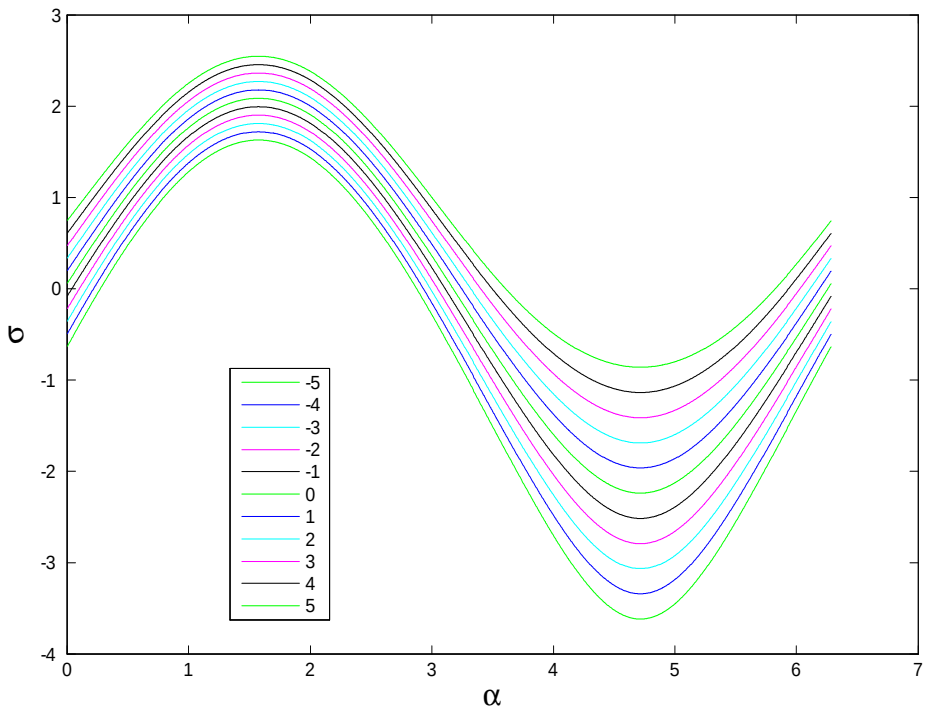

Figure 2.12: σ vs. α corresponding to values of Γ_T as given in the legend, with $N = 2048$, $\mu = 2$. The larger Γ_{T} values correspond to the larger $\sigma\,(\alpha)$ values.

Chapter 3

Numerical Methods

3.1 Integral Approximations

At each time-step, the velocity field $\mathbf{u}(\mathbf{x}, t)$ will be evaluated at the point-vortices' locations $\mathbf{x} = \mathbf{x}_j$, $j = 1, 2, .., N$. $\mathbf{u}_j = \mathbf{u}(\mathbf{x}_j, t)$ will be approximated by integrating the right-hand side of (2.5) via the Trapezoidal rule, without, and then with correction terms added. A fourth-order Runge-Kutta method is used to integrate the system of ODEs (2.5) in time.[1] Without the correction terms added, the integral approximation is $O\left(\frac{1}{N}\right)$. With the correction terms added, the integral approximation is exponentially accurate. However, the integral approximations lose their accuracy near the time of singularity formation.

[1] Another method used by Shelley [26], termed the modified point-vortex approximation, which does not use correction terms, but is also exponentially accurate, can also be used.

3.1.1 Without Correction Terms

Let us approximate the right-hand side of (2.5) by the Trapezoidal rule. We need to drop the $j = k$ contribution in the principle-value integrals so that they can be integrated. Figure 3.1 shows the estimated error of doing so, and indicates that it is a first-order approximation $O\left(\frac{1}{N}\right)$.

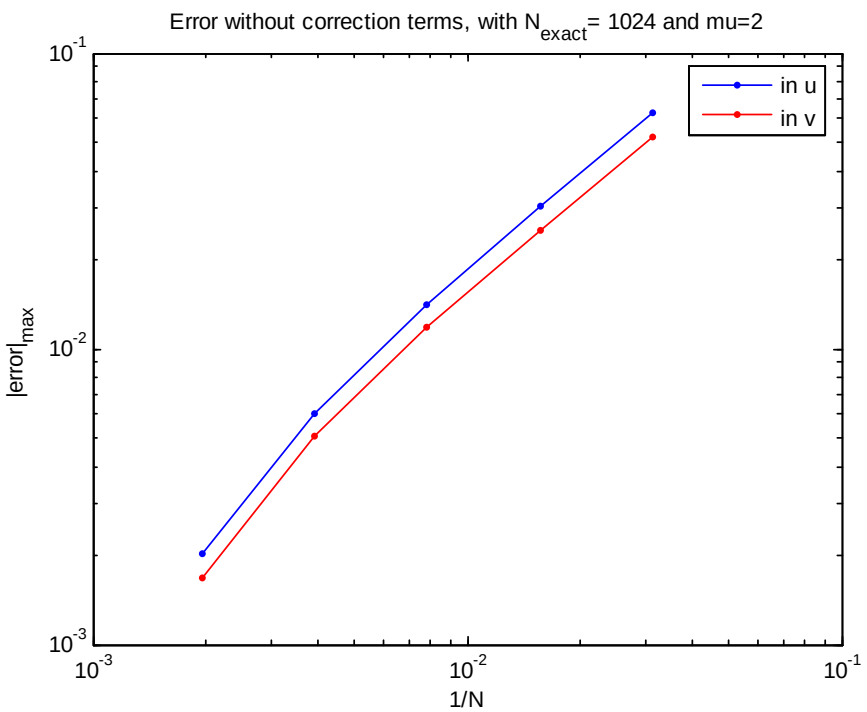

Figure 3.1: Convergence of the velocity field integrals (2.5) using the Trapezoidal rule approximation.

3.1.2 With Correction Terms

In order to gain better accuracy in the integration of the right-hand side of (2.5), we proceed to do the following [24]. Define $G^{\mathbf{u}}(\alpha,\alpha_j,t) = \begin{pmatrix} G^u(\alpha,\alpha_j,t) \\ G^v(\alpha,\alpha_j,t) \end{pmatrix}$ to be the integrands of the principal integral terms found in the velocity field $\mathbf{u}(\mathbf{x}_j,t)$ given in (2.5). They are $G^{\mathbf{u}}(\alpha,\alpha_j,t) = \frac{1}{(x_j-x)^2+(y_j-y)^2}\begin{pmatrix} y_j-y \\ x_j-x \end{pmatrix}\Gamma'(\alpha)$, where we note that $\mathbf{x} = \mathbf{x}(\alpha,t)$ and $\mathbf{x}_j = \mathbf{x}(\alpha_j,t)$. $\mathbf{G}^{\mathbf{u}}(\alpha,\alpha_j,t)$ can be expanded in $\alpha-\alpha_j$ of the form $\frac{c_{-1}^{\mathbf{u}}}{\alpha-\alpha_j} + \tilde{G}^{\mathbf{u}}(\alpha,\alpha_j,t)$, where $\tilde{G}^{\mathbf{u}}(\alpha,\alpha_j,t) = \sum_{n=0}^{\infty} c_n^{\mathbf{u}}(\alpha-\alpha_j)^n$, $c_n^{\mathbf{u}} = \begin{pmatrix} c_n^u(\alpha_j,t) \\ c_n^v(\alpha_j,t) \end{pmatrix}$. Note that $\tilde{G}^{\mathbf{u}}(\alpha_j,\alpha_j,t) = \begin{pmatrix} c_0^u \\ c_0^v \end{pmatrix}$. According to [24], we can make the approximation

$$P.V.\int_0^{2\pi} G^{\mathbf{u}}(\alpha,\alpha_j,t)\,d\alpha \approx (\alpha-\alpha_j)\sum_{k\neq j}{}' G^{\mathbf{u}}(\alpha_k,\alpha_j,t) + (\alpha-\alpha_j)\,\tilde{G}^{\mathbf{u}}(\alpha_j,\alpha_j,t)\,, \quad (3.1)$$

where the $\sum'$ denotes that the first and last summations are multiplied by $\frac{1}{2}$. The first term is the Trapezoidal rule for the principal-value integrals, and the second term a correction term. We need now solve for $G^{\mathbf{u}}(\alpha_j,\alpha_j,t)$ in order to perform this approximation, which we will now do.

Using a Taylor series expansion about $\alpha=\alpha_j$, we have

$$\begin{aligned} \mathbf{x}(\alpha) &= \mathbf{x}(\alpha_j) + \mathbf{x}'(\alpha_j)(\alpha-\alpha_j) + \frac{\mathbf{x}''(\alpha_j)}{2}(\alpha-\alpha_j)^2 + ..., \quad (3.2)\\ \Gamma'(\alpha) &= \Gamma'(\alpha_j) + \Gamma''(\alpha_j)(\alpha-\alpha_j) + ... \,. \end{aligned}$$

Letting $h=\alpha-\alpha_j$, $\Gamma=\Gamma(\alpha)$, and $\Gamma_j=\Gamma(\alpha_j)$; this can be rewritten as $\mathbf{x}(\alpha) = \mathbf{x}_j + \mathbf{x}_j'h + \frac{\mathbf{x}_j''}{2}h^2 + ...$, and $\Gamma' = \Gamma_j' + \Gamma_j''h + ...$. So

$$G^u(\alpha,\alpha_j,t)=\frac{y_j-y}{(x_j-x)^2+(y_j-y)^2}\Gamma'$$

$$=\frac{\left(y_j-\left[y_j+y_j'h+\frac{y_j''}{2}h^2+O\left(h^3\right)\right]\right)\left[\Gamma_j'+\Gamma_j''h+O\left(h^2\right)\right]}{\left(x_j-\left[x_j+x_j'h+\frac{x_j''}{2}h^2+O(h^3)\right]\right)^2+\left(y_j-\left[y_j+y_j'h+\frac{y_j''}{2}h^2+O(h^3)\right]\right)^2}$$

$$=\frac{\left[-y_j'h-\frac{y_j''}{2}h^2+O\left(h^3\right)\right]\left[\Gamma_j'+\Gamma_j''h+O\left(h^2\right)\right]}{\left(x_j-\left[x_j+x_j'h+\frac{x_j''}{2}h^2+O(h^3)\right]\right)^2+\left(y_j-\left[y_j+y_j'h+\frac{y_j''}{2}h^2+O(h^3)\right]\right)^2}$$

$$=\frac{\left[-y_j'h-\frac{y_j''}{2}h^2+O\left(h^3\right)\right]\left[\Gamma_j'+\Gamma_j''h+O\left(h^2\right)\right]}{\left(-x_j'h-\frac{x_j''}{2}h^2+O(h^3)\right)^2+\left(-y_j'h-\frac{y_j''}{2}h^2+O(h^3)\right)^2}$$

$$=\frac{-y_j'h\Gamma_j'+h^2\left(-\frac{y_j''}{2}\Gamma_j'-y_j'\Gamma_j''\right)+O\left(h^3\right)}{h^2\left(x_j^2+y_j^2\right)+h^3\left(x_j'x_j''+y_j'y_j''\right)+O(h^4)}=\frac{-\frac{y_j'\Gamma_j'}{h}-\left(\frac{y_j''}{2}\Gamma_j'+y_j'\Gamma_j''\right)+O(h)}{\left(x_j^2+y_j^2\right)+h\left(x_j'x_j''+y_j'y_j''\right)+O(h^2)}$$

$$=\frac{1}{x_j'^2+y_j'^2}\left[1-\frac{\left(x_j'x_j''+y_j'y_j''\right)h}{x_j'^2+y_j'^2}+O\left(h^2\right)\right]\left[\frac{-y_j'\Gamma_j'}{h}-\frac{y_j''\Gamma_j}{2}-y_j'\Gamma_j''+O\left(h\right)\right].$$

And,

$$G^v(\alpha,\alpha_j,t)=\frac{x_j-x}{(x_j-x)^2+(y_j-y)^2}\Gamma'$$

$$=\frac{\left(x_j-\left[x_j+x_j'h+\frac{x_j''}{2}h^2+O\left(h^3\right)\right]\right)\left[\Gamma_j'+\Gamma_j''h+O\left(h^2\right)\right]}{\left(x_j-\left[x_j+x_j'h+\frac{x_j''}{2}h^2+O(h^3)\right]\right)^2+\left(y_j-\left[y_j+y_j'h+\frac{y_j''}{2}h^2+O(h^3)\right]\right)^2}$$

$$=\frac{\left[-x_j'h-\frac{x_j''}{2}h^2+O\left(h^3\right)\right]\left[\Gamma_j'+\Gamma_j''h+O\left(h^2\right)\right]}{\left(x_j-\left[x_j+x_j'h+\frac{x_j''}{2}h^2+O(h^3)\right]\right)^2+\left(y_j-\left[y_j+y_j'h+\frac{y_j''}{2}h^2+O(h^3)\right]\right)^2}$$

$$=\frac{\left[-x_j'h-\frac{x_j''}{2}h^2+O\left(h^3\right)\right]\left[\Gamma_j'+\Gamma_j''h+O\left(h^2\right)\right]}{\left(-x_j'h-\frac{x_j''}{2}h^2+O(h^3)\right)^2+\left(-y_j'h-\frac{y_j''}{2}h^2+O(h^3)\right)^2}$$

$$=\frac{-x_j'h\Gamma_j'+h^2\left(-\frac{x_j''}{2}\Gamma_j'-x_j'\Gamma_j''\right)+O\left(h^3\right)}{h^2\left(x_j^2+y_j^2\right)+h^3\left(x_j'x_j''+y_j'y_j''\right)+O(h^4)}=\frac{-\frac{x_j'\Gamma_j'}{h}-\left(\frac{x_j''}{2}\Gamma_j'+x_j'\Gamma_j''\right)+O(h)}{\left(x_j^2+y_j^2\right)+h\left(x_j'x_j''+y_j'y_j''\right)+O(h^2)}$$

$$=\frac{1}{x_j'^2+y_j'^2}\left[1-\frac{\left(x_j'x_j''+y_j'y_j''\right)h}{x_j'^2+y_j'^2}+O\left(h^2\right)\right]\left[-\frac{x_j'\Gamma_j'}{h}-\left(\frac{x_j''}{2}\Gamma_j'+x_j'\Gamma_j''\right)+O\left(h\right)\right].$$

We noted that

$$\left(-x'_j h - \tfrac{x''_j}{2}h^2\right)^2 + \left(-y'_j h - \tfrac{y''_j}{2}h^2\right)^2$$

$$= h^2 x'^2_j + h^3 x'_j x''_j + \tfrac{1}{4}h^4 x''^2_j + h^2 y'^2_j + h^3 y'_j y''_j + \tfrac{1}{4}h^4 y''^2_j$$

$$= h^2\left(x'^2_j + y'^2_j\right) + h^3\left(x'_j x''_j + y'_j y''_j\right) + O\left(h^4\right), \text{ and}$$

$$\frac{1}{\left(x_j^2+y_j^2\right)+h\left(x'_j x''_j + y'_j y''_j\right)+O(h^3)} = \frac{1}{x'^2_j + y'^2_j}\left(1 - \frac{\left(x'_j x''_j + y'_j y''_j\right)h}{x'^2_j + y'^2_j} + O\left(h^2\right)\right).$$

It follows that[2]

$$\tilde{G}^{\mathbf{u}}\left(\alpha_j, \alpha_j, t\right) = \begin{pmatrix} c_0^u \\ c_0^v \end{pmatrix} = \begin{pmatrix} \frac{1}{x'^2_j + y'^2_j}\left[\frac{y'_j \Gamma'_j\left(x'_j x''_j + y'_j y''_j\right)}{x'^2_j + y'^2_j} - \frac{y''_j}{2}\Gamma'_j - y'_j \Gamma''_j\right] \\ \frac{1}{x'^2_j + y'^2_j}\left[\frac{x'_j \Gamma'_j\left(x'_j x''_j + y'_j y''_j\right)}{x'^2_j + y'^2_j} - \frac{x''_j}{2}\Gamma'_j - x'_j \Gamma''_j\right] \end{pmatrix}. \quad (3.3)$$

We used the Trapezoidal rule for the approximation of the integration of the non-principal-value integrals on the right-hand side of (2.5), and (3.1) for the approximation of the integration of the principal-value integrals on the right-hand side of (2.5). The derivatives $\mathbf{x}'_j$, $\mathbf{x}''_j$, and Γ''_j are taken with respect to α; and in the simulations are computed via spectral differentiation.

With these integral approximations, we get exponential decay in the estimated error of $\mathbf{u}_j$ as N is increased, up to almost the magnitude of the set level of the Fourier filter [3], which is 10^{-12} in this case. This can be observed in Figure 3.2 for $t = 0$, and in Figure 3.3 for the later time $t = 0.2$. This is a nice improvement from the errors in the integral approximations with the use of the Trapezoidal rule without the correction terms, as shown in Figure 3.1. Note that some of the higher error in Figure 3.3 is due to newly introduced errors in the computed positions $\mathbf{x}_j$ as time is incremented, and are in part due to the implementation of the Fourier filter. Van de Vooren [28] is responsible for this method of integral approximation.

[2] Recall that $\Gamma'_j = \sigma_j$.

[3] The Fourier filter will be described shortly.

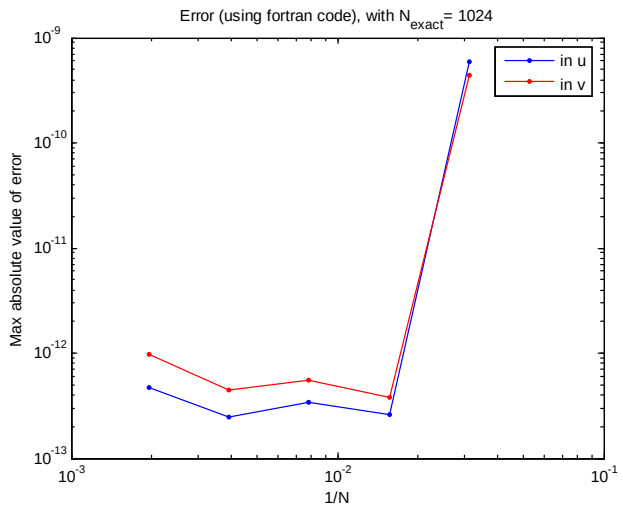

Figure 3.2: Convergence of the velocity field integrals (2.5) using the Trapezoidal rule plus correction terms, at $t = 0$.

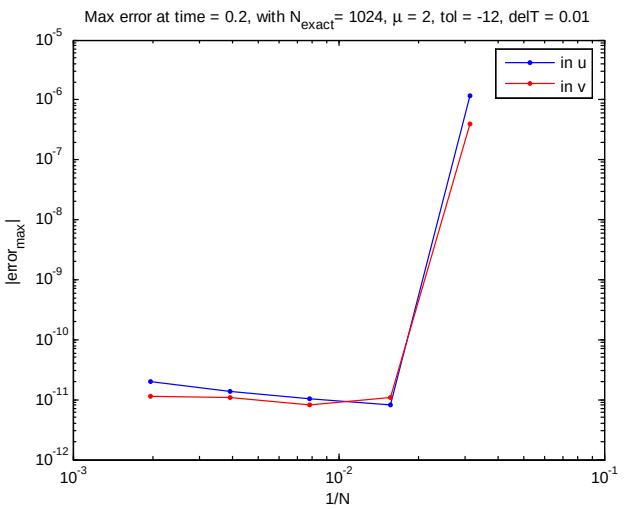

Figure 3.3: Convergence of the velocity field integrals (2.5) using the Trapezoidal rule plus correction terms, at $t = 0.2$.

3.2 Irregular Point-Vortex Motion, Computer Precision, and Krasny's Fourier Filter

Prior to the critical times, irregular point motion can occur in the positions of the point-vortices used in approximating vortex sheets. Figure 3.4 and Figure 3.5 demonstrate this occurrence with respect to our problem. Krasny [13] serves as one of the classic references on this topic.

Irregular point motion in the discretized vortex sheets is due to the growth of computer discretization/round-off error resulting from Kelvin-Hemholtz instability. An increase in machine precision can help control this irregular motion, yet it comes at a computational cost. Observe that for fixed $N = 256$, $\Delta T = 0.01$, and $\mu = 2$, irregular point motion decreases in our problem when changing from single to double machine precision (Figures 3.4 and 3.5).[4] The implementation of a Fourier filter is another way to control the irregular point motion. Known as Krasny's Fourier filter, it sets all modes in the point-vortices' positions below a designated filter level to zero. The designated filter level is either referred to as l or tol in this paper; l implying a filter level of a value of 10^{-l}, and tol being equal to 10^{-l}. Setting the filter level needs to be done in a manner so that the high modes in the discretization/round-off error cannot grow due to Kelvin-Hemholtz instability [13] [24]. To implement the Fourier filter, at each timestep the Fourier transform to the point-vortices' positions is taken, the filter applied to the Fourier coefficients, and the inverse Fourier transform then taken. The difference between Figure 3.5 (without the Fourier filter) with that of Figure 3.7 (with the Fourier filter) demonstrates the effects of using the filter in instance of the double machine precision. Also, the irregular point motion is not due to a lack in resolution of time. This can be observed in the comparison of Figure 3.5 with that of Figure 3.6; the corresponding timesteps are $\Delta T = 0.01$ and

[4] ΔT denotes the timestep used in the sheet evolution.

$\Delta T = 0.001$, respectively.

Since the irregular point motion increases with an increase in N, error in the sheet evolution will also increase with increased N. So, the level of the Fourier filter needs to simultaneously be made smaller as N is increased in order to reduce the overall error [2] [13] [24]. The Fourier filter does introduce an error that is dependent on both the timestep and the filter level. So for increased precision, the Fourier filter level can be set at a lower level; this would result in a smaller error contribution. The vortex sheet simulations incorporating the Fourier filter were done in double (with $l = 10$ to $l = 13$) or quadruple (with $l = 28$) precision in the following sections of this paper.

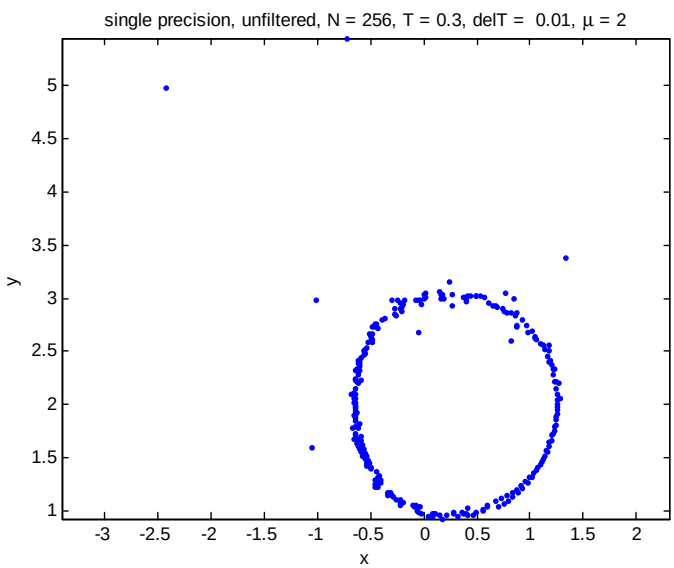

Figure 3.4: Locations of point-vortices used to approximate vortex sheet, using single precision, without a Fourier filter, and with $N = 256$, $t = 0.3$, $\Delta T = 0.01$, $\mu = 2$.

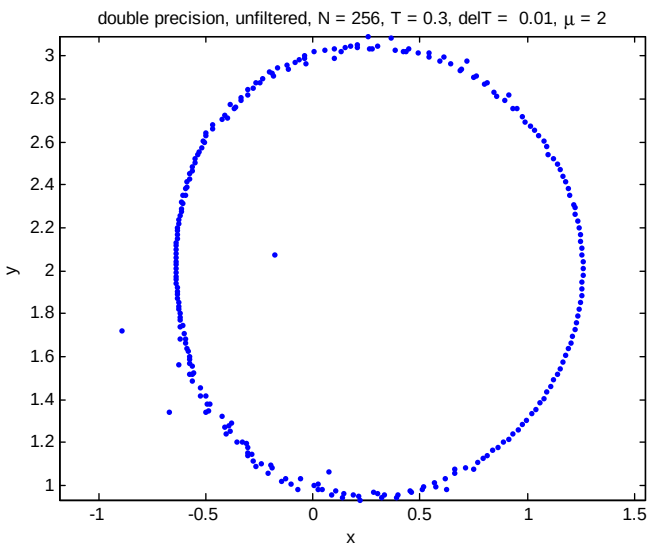

Figure 3.5: Locations of point-vortices used to approximate vortex sheet, using double precision, without a Fourier filter, and with $N = 256$, $t = 0.3$, $\Delta T = 0.01$, $\mu = 2$.

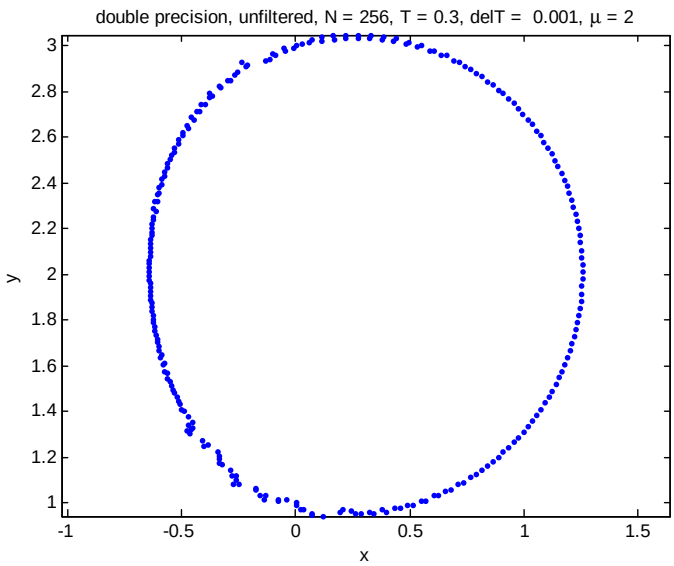

Figure 3.6: Locations of point-vortices used to approximate vortex sheet, using double precision, without a Fourier Filter, and with $N = 256$, $t = 0.3$, $\Delta T = 0.001$, $\mu = 2$.

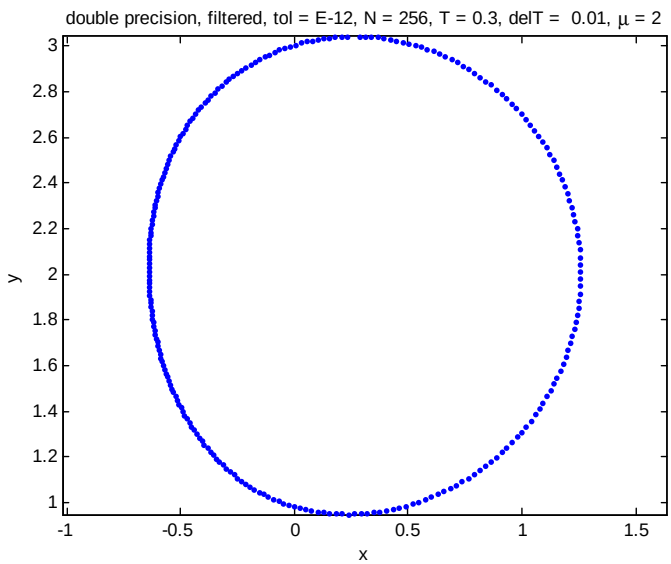

Figure 3.7: Locations of point-vortices used to approximate vortex sheet, using double precision and the Fourier filter set to $l = 12$, with $N = 256$, $t = 0.03$, $\Delta T = 0.01$, $\mu = 2$.

Chapter 4

Evolution Results

4.1 Evolution of Vortex Sheet, Curvature, and Critical Times Estimates

Figure 4.1 shows snapshots at the specified times for the evolution of the top and bottom vortex sheets, where $N = 512$, $\mu = 2$, the filter level $l = 12$, and the timestep $\Delta T = 0.001$. The bottom vortex sheet is the a mirror image of the top sheet about the x-axis. The bottom sheet in Figure 4.1 shows the every fourth point vortices used in the sheet approximation in order to show how the point-vortices move on the sheet. The top sheet shows the interpolating curve of the point-vortices used in the approximation. The point-vortices do not remain uniformly spaced throughout the sheet, but instead become more bunched towards the rear of the sheet, and less bunched towards the front of the sheet, as is increased. These computations were performed in double precision. Recall that the sheets were initially given a velocity of $\mathbf{U} = (1, 0, 0)$. Thus, the fronts of the sheets are thought of as being the rightmost parts. Nitsche provides an explanation of why the sheet rolls up as shown, "The front vorticity causes vortex elements in the rear to decrease in radius, while the rear

vorticity causes vortex elements in the front to increase in radius. Since elements with smaller radii travel faster, the rear elements move towards the front ones and the shape of the vortex sheets becomes narrower" [24].

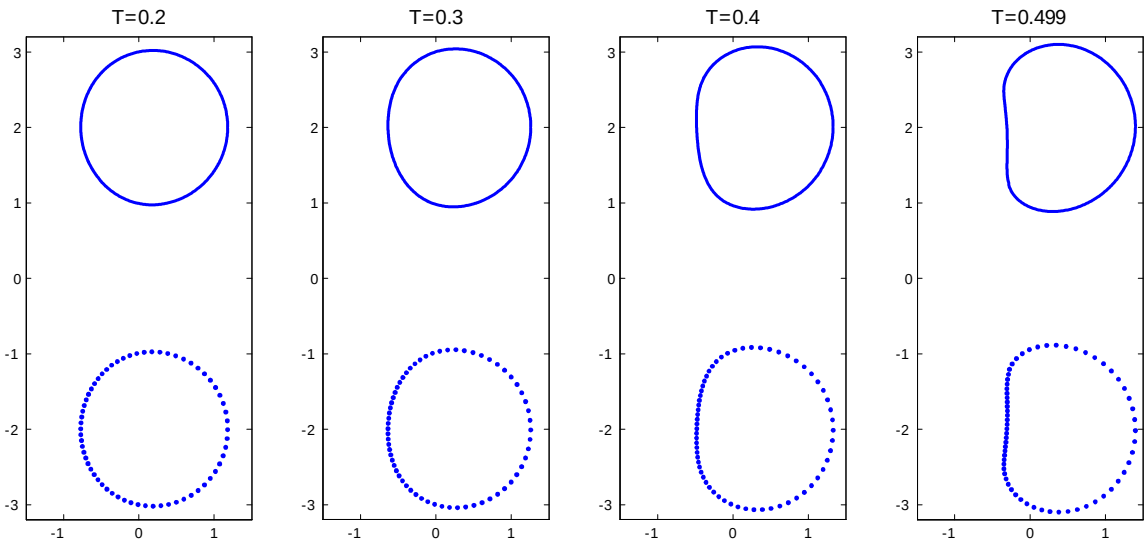

Figure 4.1: Computed evolution of the top and bottom vortex sheets at the listed times, with $N = 512$, $\mu = 2$, $l = 12$, $\Delta T = 0.001$.

Singularities which form are infinite jump discontinuities in the curvature of the vortex sheet [18] [10] [13]. These singularities occur in the vortex sheets at finite times, are called the critical times, and are denoted by t_c. The point-vortex approximation converges up to but not beyond these critical times. Thus, knowing when critical times occur is an important consideration in vortex sheet evolution.

The curvature of the vortex sheet is given by

$$\kappa(\alpha, t) = \frac{x_\alpha y_{\alpha\alpha} - x_{\alpha\alpha} y_\alpha}{(x_\alpha^2 + y_\alpha^2)^{\frac{3}{2}}} \tag{4.1}$$

Let $\kappa_{\max}(t)$ denote the maximum curvature of the vortex sheet at time t. The

critical times can be estimated as the time limit in which $\frac{1}{\kappa_{\max}(t)}$ approaches zero. Figure 4.2 plots $\frac{1}{\kappa_{\max}(t)}$ for specified l values (filter level is 10^{-l}) and N values, for $\mu = 2$. Note that for all α, $\kappa(\alpha, 0) = 1$. Figure 4.3 is a close-up of Figure 4.2, where the filter level and N are taken to increase from right to left in these plot. Both of these plots support the notion that the critical times occur at a finite time. Observe in these figures that $\frac{1}{\kappa_{\max}(t)}$ approaches zero at earlier times as l and N are increased. Thus, critical time estimates taken from these plots will be a slight overshoot of the actual critical times. Better critical time estimates could be obtained from increasing l and N further.

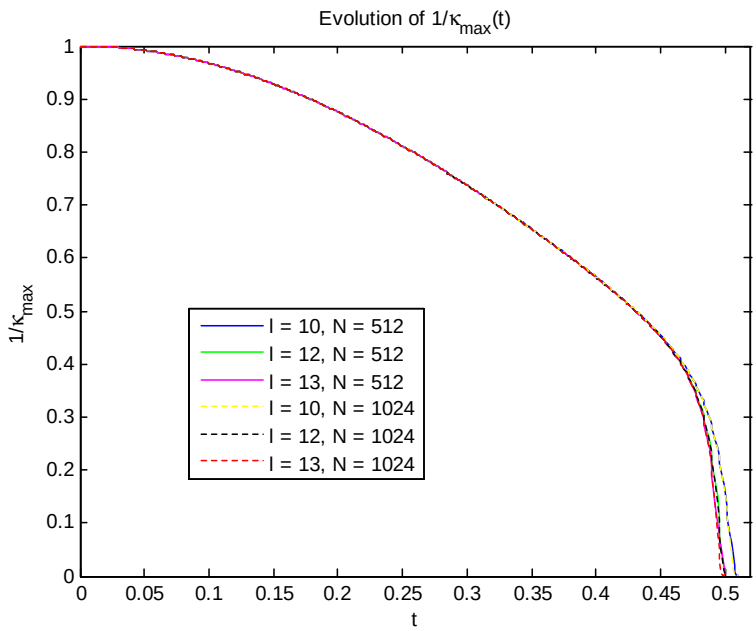

Figure 4.2: Plot of $\frac{1}{\kappa_{\max}}$ vs. t, for specified l and N values, for $\mu = 2$, $\Gamma_T = 0$.

Another method that can be used to estimate critical times monitors when a kink[1] forms in the vortex sheets' geometry. When a kink has formed, we know

[1]We define the occurrence of a kink as when, for two adjacent point vortices, one point-vortex passes vertically over the other one.

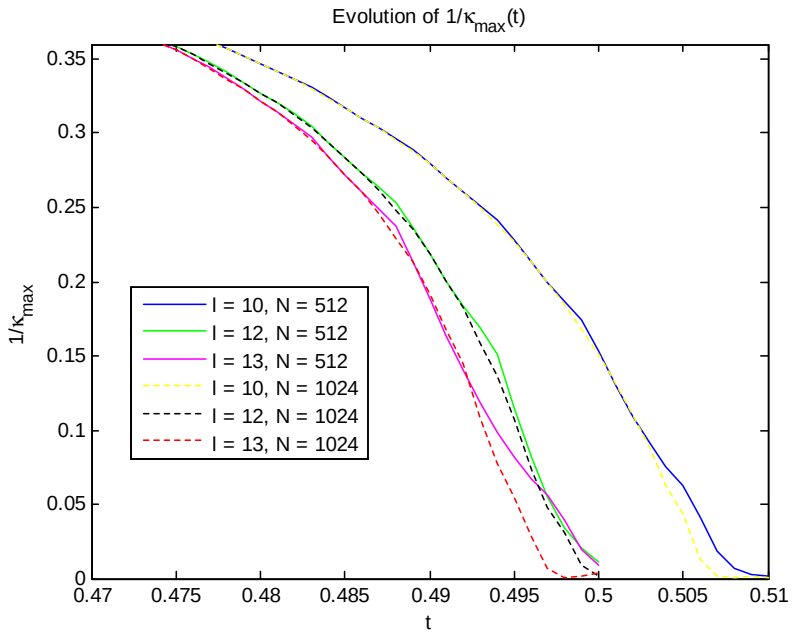

Figure 4.3: Closeup of $\frac{1}{\kappa_{\max}}$ vs. t, for specified l and N values, near the critial time, for $\mu = 2$, $\Gamma_T = 0$.

that a singularity has occurred a short time beforehand. The location of singularity formation can also be estimated by the location of the kink. The method consists of the following: If the two conditions are satisfied (where $\mathbf{x}_j$, $j = 1, 2, ..., N$, denote the point-vortices' locations)

- $y_j < c$, for some appropriately chosen constant c (so as to choose a particular region of the sheet)
- $x_j > \max(x_{j+1}, x_{j-1})$,

then a singularity has formed in a small neighborhood about $\mathbf{x}_j$.

This method only roughly approximates the time of singularity formation. Again, it is an overshoot of the actual critical times. This overshoot is partly due to the

discretization of the vortex sheet. Also, according to Krasny, the singularity is not actually visually apparent in the vortex sheet at the critical time. And in the limit $N \to \infty$, there will actually be no kink formation in the sheet at the critical time [13].

The geometries of the top vortex sheets at the kink critical time estimates are shown in Figure 4.4 for several μ and Γ_T values, with $N = 512$, $l = 28$, $\Delta T = 0.001$. Do not forget that there is a bottom sheet as well; we simply did not include it in the plots because no new information is gained in doing so. The approximate location at which the singularity formation occurs is indicated on these plots by the diamond shaped marker. Varying Γ_T will affect the geometries of the vortex sheets' evolution, location of singularity formation, and critical times. Observe that the singularity is located on the bottom half of the vortex sheet in the plots for $\Gamma_T = -5$ and 0, and on the upper half of the sheet for $\Gamma_T = 5$.

Observe that the singularity location moves down on the sheet (that is, towards the x-axis) as μ decreases, for $\Gamma_T = -5$ and 0; and up along the sheet (that is, away from the x-axis) as μ decreases, for $\Gamma_T = 5$. In the limiting case of one vortex sheet (i.e. $\mu \to \infty$), Nitsche found that two symmetric singularities will occur simultaneously on the vortex sheet, with one located on the bottom half of the sheet, and one located on the top half of the sheet [24]. More on the effects of Γ_T in the sheet evolutions can be seen in Chapter 6.

Figure 4.5 plots the estimated critical times using the kink method, for specified μ and N values, for $\Gamma_T = 0$. This figure shows that in general, the critical time estimates decrease as N increases and as μ decreases. Figure 4.6 plots the kink estimated critical times t_c vs. μ for several different values of Γ_T, where $N = 512$, $\Delta T = 0.001$, and $l = 28$.[2] The value $t_c = 0.587$ corresponding to $\mu = 5$, $\Gamma_T = 0$

[2]Note that these computations were performed in quadrupole precision, allowing the specified filter level l.

appears to be in close agreement with the value of $t_c = 0.5825$ given in the limiting case $\mu \to \infty$ given by Nitsche[3] in [24]. Define α_c to be the value of the Lagrangian parameter α corresponding to the location of the singularity on the vortex sheet at time t_c. Figure 4.7 plots the kink estimated α_c values for specified μ and Γ_T values, where $N = 512$, $\Delta T = 0.001$, and $l = 28$. The value $\alpha_c = 4.050$ corresponding to $\mu = 5$, $\Gamma_T = 0$ appears to also be in close agreement with the value of $\alpha_c = 3.927$ given in the limiting case $\mu \to \infty$ given by Nitsche in [24].[4]

The two presented critical time estimation methods are rough estimates. A more precise method that will yield greater insight into critical time estimation, as well as other characteristics of the singularity formation is forthcoming.

[3]Note that in [24], Nitsche uses a different nondimensionalized velocity U different than ours. We must divide her value of t_c by 4 to arrive at the value corresponding to the t_c relevant to our sheets.

[4]Note that in [24], Nitsche uses a different parameterization than us, and so the α_c given in her paper as 0.75π corresponds to an $\alpha_c = 2\pi - 0.75\pi$ in our problem.

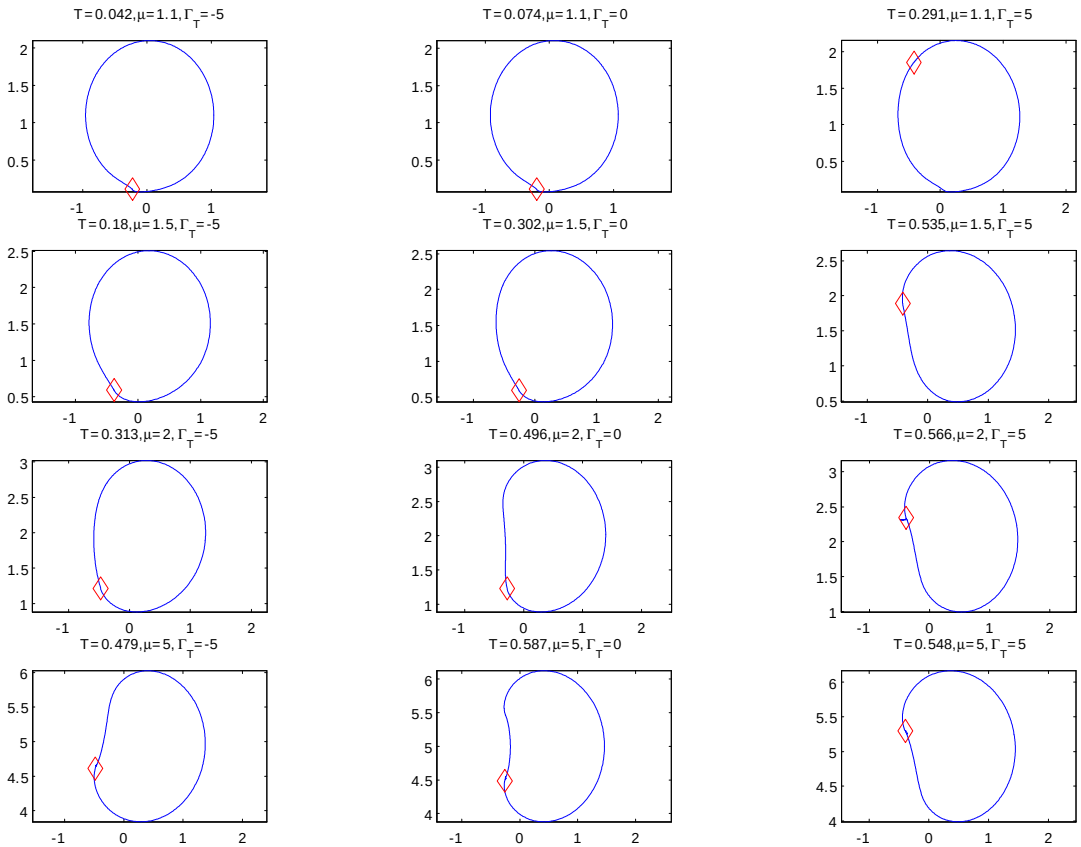

Figure 4.4: Computed top vortex sheet for specified μ and Γ_T values at the kink critical time estimates, where $N = 512$, $l = 28$, $\Delta T = 0.001$.

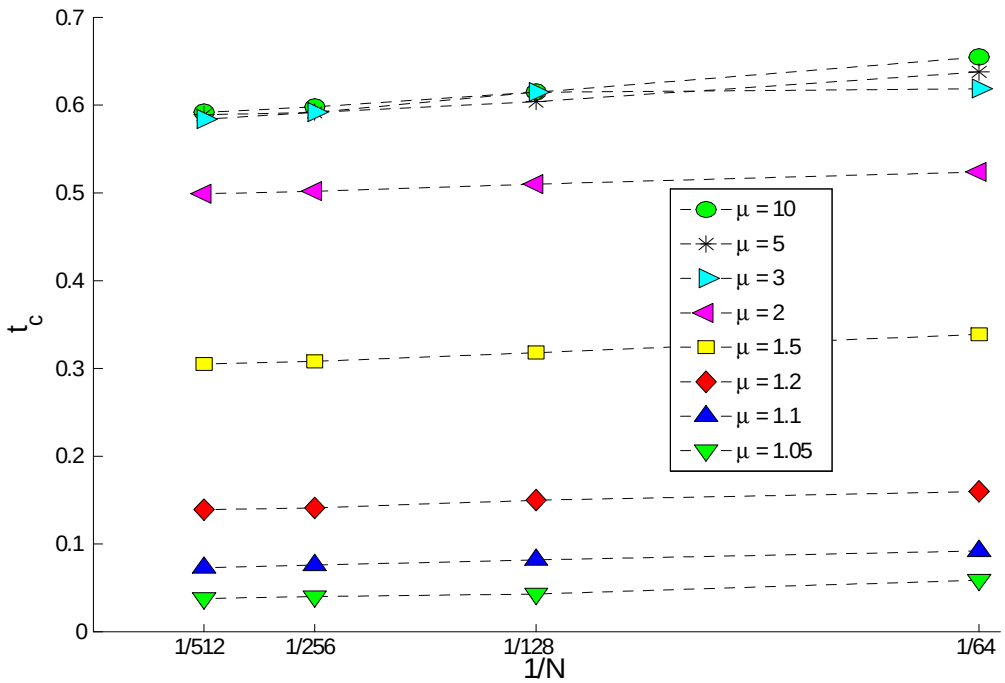

Figure 4.5: Kink estimated t_c vs. $\frac{1}{N}$, for specified μ values, with $\Gamma_T = 0$, $l = 12$, $\Delta T = 0.001$. The critical times t_c increase for increasing μ.

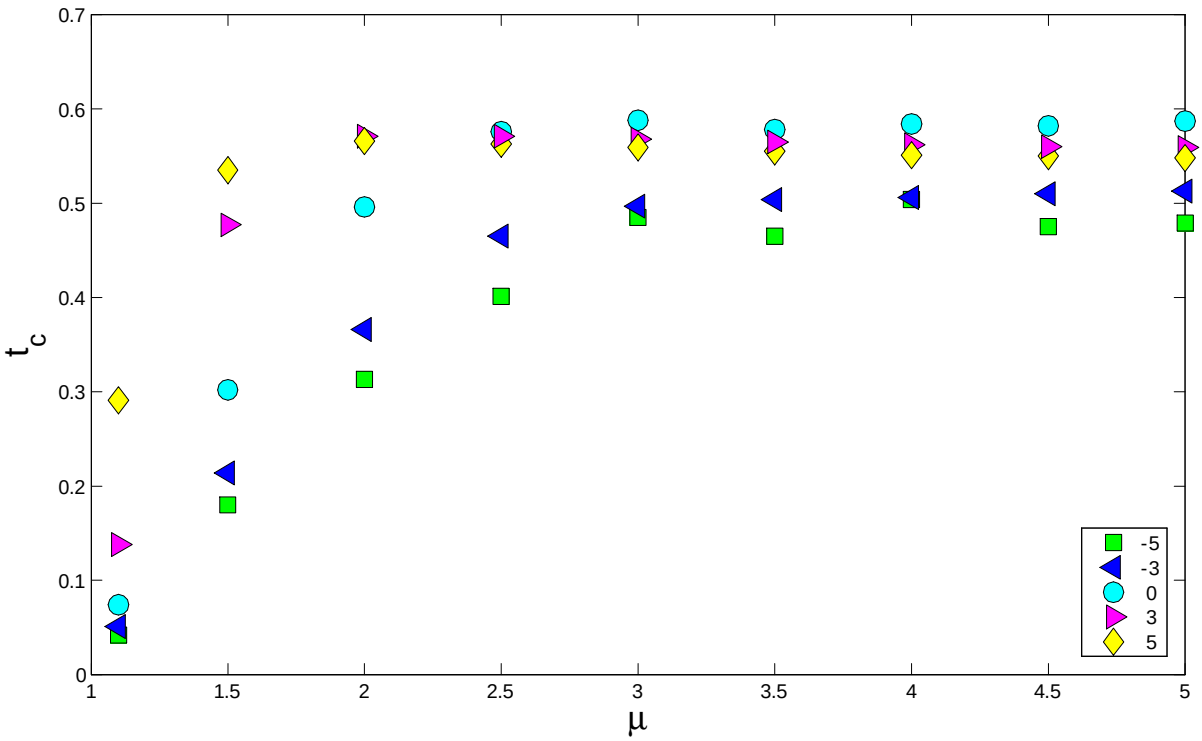

Figure 4.6: Kink estimated critical times for specified μ and Γ_T values, with $N = 512$, $\Delta T = 0.001$, $l = 28$. The legend values correspond to Γ_T values.

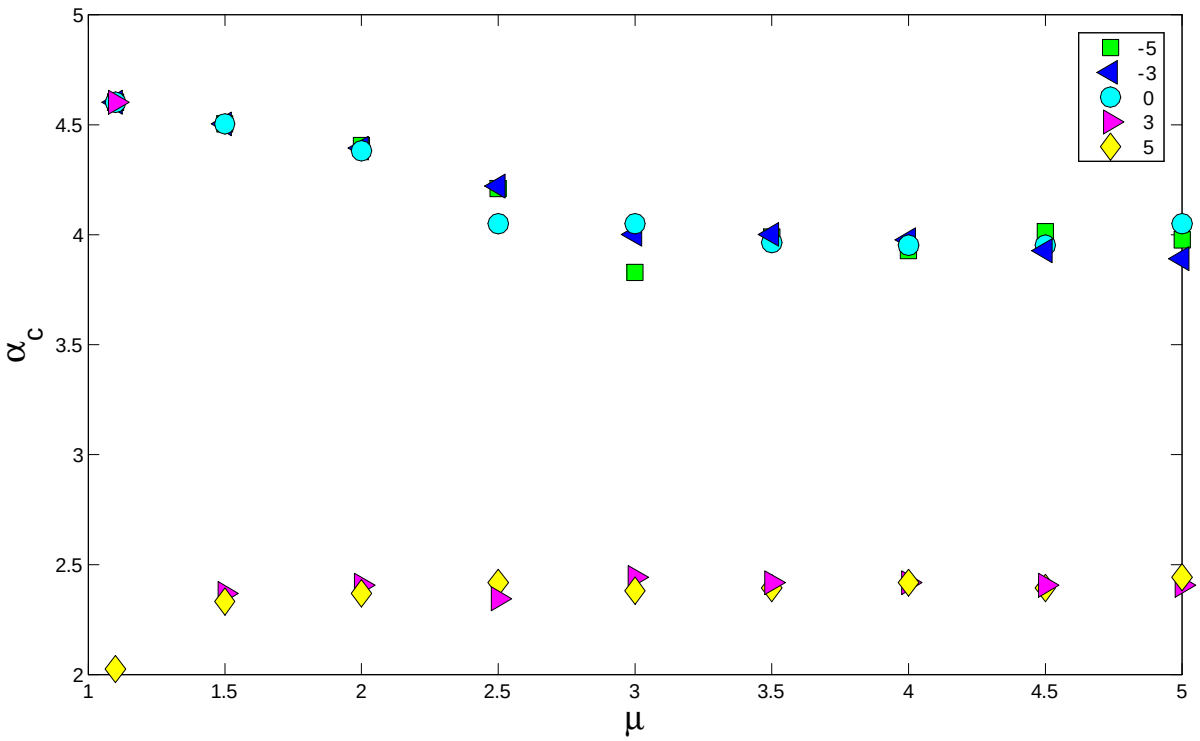

Figure 4.7: Kink estimated α_c vs. μ for the indicated Γ_T values, with $N = 512$, $\Delta T = 0.001$, $l = 28$. The legend corresponds to Γ_T values.

Chapter 5

Analysis of the Fourier Spectrum

We now turn to studying the singularity formation in more detail using the asymptotics of the Fourier coefficients corresponding to the positions of the vortex sheets [27] [24] [13] [10]. After the asymptotic expressions are developed, a linear least-squares fitting is performed over a set of the parameters included in the expressions. Confirmation that the branch point singularities are of order $\frac{3}{2}$ is one aim. Another is improved estimates of the previously approximated critical times and singularity formation locations.

5.1 Asymptotics of Fourier Integrals using Laplace's Method

The following developed derivation will be needed in the next section. This section relies significantly on a similar derivation given in Carrier, Krook, and Pearson [3, p. 255-56].[1]

[1]Here we are deriving the asymptotic expression for c_k. Carrier, Krook, and Pearson [3] gave the major steps for the derivation of the asymptotic expression for c_{-k}.

Consider the Fourier integral $I(k) = \int_{-\infty}^{\infty} e^{-ikz} f(z)\ dz$, $k \in \mathbb{N}$, where the path of integration passes above the singularities at z_j and below the singularities at ζ_j, as given in Figure 5.1.

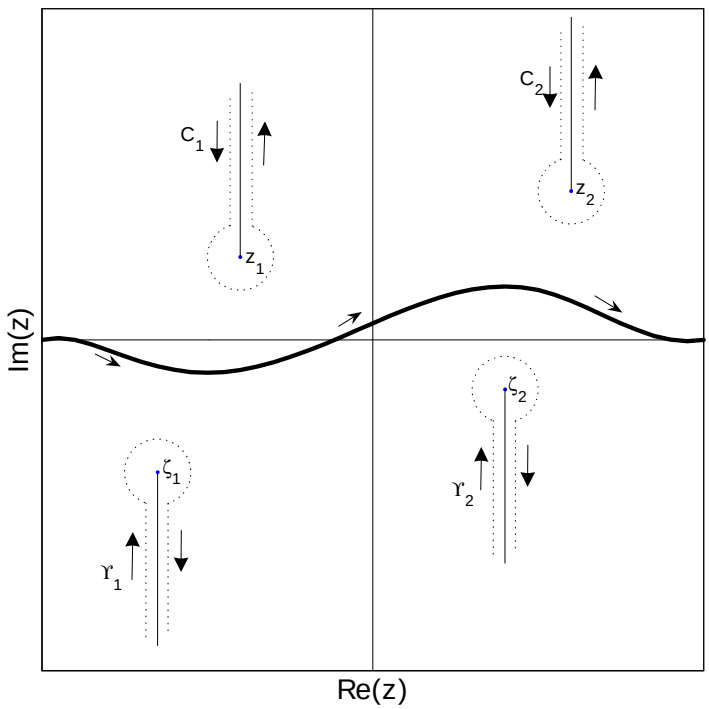

Figure 5.1: The arrows indicate the contour directions. The branch cuts extend outward from the singularities z_j and ζ_j, $j = 1, 2$.

Suppose that in a neighborhood of z_j,

$$f(z) = (z - z_j)^{\nu} \sum_{n=0}^{\infty} a_n (z - z_j)^n, \tag{5.1}$$

where $\operatorname{Re} \nu > -1$, and $|f(z)| \to 0$ uniformly as $z \to \infty$. Then by using Jordan's lemma and the Cauchy-Goursat theorem,

$$I(k) = \int_{C_1 + C_2} e^{-ikz} f(z)\ dz. \tag{5.2}$$

The contribution from C_j to $I(k)$ is given by

$$\begin{aligned}
I_{C_j}(k) &= \int_{C_j} e^{-ikz}(z-z_j)^{\nu}\left[\sum_{n=0}^{\infty} a_n (z-z_j)^n + R_N(z)\right] dz \\
&= \int_{C_{j_{\text{up}}}} e^{-ikz}(z-z_j)^{\nu}\left[\sum_{n=0}^{\infty} a_n (z-z_j)^n + R_N(z)\right] dz \\
&\quad + \int_{C_{j_{\text{down}}}} e^{-ikz}(z-z_j)^{\nu}\left[\sum_{n=0}^{\infty} a_n (z-z_j)^n + R_N(z)\right] dz \\
&= -\int_0^{\infty} e^{-ik(z_j-ir)} e^{i\frac{3\pi}{2}\nu} r^{\nu}\left[\sum_{n=0}^{\infty} a_n (-i)^n r^n + R_N(z_j-ir)\right](-i)\ dr \\
&\quad + \int_0^{\infty} e^{-ik(z_j-ir)} e^{-i\frac{\pi}{2}\nu} r^{\nu}\left[\sum_{n=0}^{\infty} a^n (-i)^n r^n + R_N(z_j-ir)\right](-i)\ dr \qquad (5.3) \\
&= i\left(e^{i\frac{3\pi}{2}\nu} - e^{-i\frac{\pi}{2}\nu}\right) e^{-ikz_j}(-1)^{\nu}\int_0^{\infty} e^{-kr} r^{\nu}\left[\sum_{n=0}^{\infty} a^n (-i)^n r^n + R_N(z_j-ir)\right] dr \\
&= -2\frac{(e^{i\pi\nu} - e^{-i\pi\nu})}{2i} e^{i\frac{\pi}{2}\nu} e^{-ikz_j} e^{i\pi\nu}\int_0^{\infty} e^{-kr} r^{\nu}\left[\sum_{n=0}^{\infty} a^n (-i)^n r^n + R_N(z_j-ir)\right] dr \\
&= -2\sin(\pi\nu)\, e^{\left(-ikz_j + i\frac{3\pi}{2}\nu\right)}\int_0^{\infty} e^{-kr} r^{\nu}\left[\sum_{n=0}^{\infty} a^n (-i)^n r^n + R_N(z_j-ir)\right] dr,
\end{aligned}$$

where we let $z = z_j - ir$. Then by Watson's lemma, for $|k|$ large we have

$$I_{C_j}(k) \sim -2\sin(\pi\nu)\, e^{\left(-ikz_j + i\frac{3\pi}{2}\nu\right)}\sum_{n=0}^{\infty} a^n (-i)^n \frac{\Gamma(\nu+n+1)}{k^{\nu+n+1}}. \qquad (5.4)$$

For $|k|$ large, $I(k)$ is dominated by the particular $I_{C_j}(k)$ with the greatest[2] $\operatorname{Im} z_j$. This can easily be seen by considering the dominant term e^{-ikz_j} in the above expression, and noting that $e^{-ikz_j} = e^{-ik\operatorname{Re}(z_j)} e^{k\operatorname{Im}(z_j)}$. So we may write

$$I(k) \sim -2\sin(\pi\nu)\, e^{\left(-ik\tilde{z} + i\frac{3\pi}{2}\nu\right)}\sum_{n=0}^{\infty} a^n (-i)^n \frac{\Gamma(\nu+n+1)}{k^{\nu+n+1}}, \qquad (5.5)$$

[2] 'greatest' is not to be taken in the $|\operatorname{Im} z_j|$ sense. For example, if $\forall j,\ z_j < 0$, then the z_j with 'greatest' imaginary part would be the one with least negative value.

where $\tilde{z}$ is now the particular z_j with 'greatest' imaginary part, assuming such a $\tilde{z}$ exists. Now if we let $n = 0$, then we have[3]

$$I(k) \sim -\frac{2a_0 \sin(\pi\nu)\,\Gamma(\nu+1)}{k^{\nu+1}} e^{\left(-ik\tilde{z}+i\frac{3\pi}{2}\nu\right)}. \tag{5.6}$$

5.2 Asymptotics Applied to the Fourier Spectrum of the Vortex Sheets' Positions

Let $f(\alpha,t) = x(\alpha,t) + iy(\alpha,t)$, where $(x(\alpha,t), y(\alpha,t))$ denotes the positions of the top vortex sheet. Assume that $f(\alpha,t)$ can be analytically continued for complex values of α to a strip of width $\eta(t)$ in either the upper or lower-half complex α plane.[4] Furthermore, suppose that this analytic continuation of $f(\alpha,t)$ contains branch point singularities of order $p > -1$ located on the upper boundary of this strip; that is, at $\alpha = \zeta \equiv \alpha_c(t) + i\eta(t)$. Then, in a neighborhood of ζ, $f(\alpha) = (\alpha-\zeta)^{\mu}\sum_{n=0}^{\infty} a^n(\alpha-\zeta)^n$, where $\mu(t) \equiv p(t) + i\nu(t)$.[5] Using the results of the previous section, for large $k > 0$ we have $c_k \sim -\frac{2a_0 \sin(\pi\mu)\Gamma(\mu+1)}{k^{\mu+1}} e^{\left(-ik\tilde{\zeta}+i\frac{3\pi}{2}\mu\right)}$. That is,

$$\begin{aligned} c_k &\sim -\frac{2a_0 \sin(\pi\mu)\,\Gamma(\mu+1)}{k^{p+i\nu+1}} e^{\left[-ik(\alpha_c+i\eta)+i\frac{3\pi}{2}(p+i\nu)\right]} \\ &= -\frac{2a_0 \sin(\pi\mu)\,\Gamma(\mu+1)\,e^{-\frac{3\pi}{2}\nu}e^{i\frac{3\pi}{2}p}}{k^{p+1}} e^{k\eta}k^{-i\nu}e^{-ik\alpha_c} = \frac{A}{k^{p+1}} e^{k\eta}k^{-i\nu}e^{-ik\alpha_c} \\ &= \frac{|A|\,e^{i\phi}}{k^{p+1}} e^{k\eta}e^{-i\nu\ln k}e^{-ik\alpha_c}, \end{aligned} \tag{5.7}$$

where $A = |A|\,e^{i\phi}$, and we let $A = -2a_0 \sin(\pi\mu)\,\Gamma(\mu+1)\,e^{-\frac{3\pi}{2}\nu}e^{i\frac{3\pi}{2}p}$.[6]

[3] See Appendix B for the similiar asymptotics derivation corresponding to c_{-k}.

[4] The strip of width $\eta(t)$ is to be in the upper-half α plane if $\eta(t) > 0$, and in the lower-half α plane if $\eta(t) < 0$.

[5] The $\mu(t)$ used here is different than the $\mu = \frac{D}{R}$ used to indicate the geometry of the two cylindrical sheets; and is used to be consistent with the work of Nitsche [24].

[6] For the limiting case $\mu \to \infty$, the reader is referred to [24] for the asymptotics fo c_k.

Taking the ln of both sides then yields

$$\ln\sqrt{a_k^2+b_k^2}+i\tan^{-1}\left(\frac{b_k}{a_k}\right)=\ln|A|+\eta k-(p+1)\ln k-i\nu\ln k-ik\alpha_c+i\phi, \quad (5.8)$$

where we have let $c_k = a_k + ib_k$.[7] Equating the real and imaginary parts of this expression then yields

$$\ln\sqrt{a_k^2+b_k^2} = \ln|A|+\eta k-(p+1)\ln k, \quad (5.9)$$

$$\tan^{-1}\left(\frac{b_k}{a_k}\right) = \phi-\nu\ln k-k\alpha_c. \quad (5.10)$$

$|A|$, p, η, ϕ, $-\nu$, and α_c are functions of k and t. If $\eta(t)\to 0$ as $t\to t_c$, there will be a change from exponential to algebraic decay in $|c_k|$. At $\eta(t_c)=0$, this algebraic decay will be of the order $p+1$ in $|c_k|$. Evidence of this decay can be observed in Figure 5.2.[8] In this plot, as time increases up to the critical time, the Fourier coefficients do indeed appear to become linear. A dashed reference line with slope -2.5 is indicated in the figure, and matches up with the general behavior of $|c_k|$ near the estimated critical time. It supports the notion that a branch point singularity with order of $\frac{3}{2}$ occurs.

As μ increases, it has been observed that oscillations in the plots of $|c_k|$ versus k will also increase, as seen by comparing Figure 5.2 with Figure 5.3. In the limiting case $\mu\to\infty$ performed by Nitsche [24], the oscillations appear to be greatest; and is shown to be due to the simultaneous formation of two singularities [24]. We think this increased oscillatory behavior as μ increases is due to the contribution of a second singularity on the same vortex sheet[9].

[7] Recall that $\ln c_k = \ln\sqrt{a_k^2+b_k^2}+i\tan^{-1}\left(\frac{b_k}{a_k}\right)$.

[8] These plots of $|c_k|$ have had the Fourier filter applied to them.

[9] More on this 2nd singularity formation will be discussed in Section 5.4.

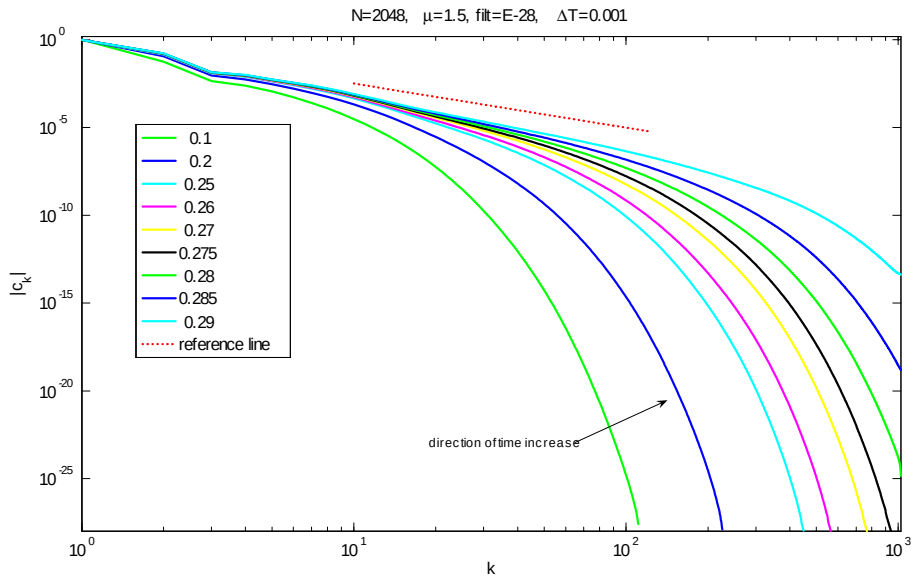

Figure 5.2: Fourier coefficients $|c_k|$ vs. k, for $\mu = 1.5$, with $\Gamma_T = 0$. The dotted reference line denotes a slope of -2.5 on the plot. The coefficients increase as time increases.

We seek the values of the parameters $|A|$, p, η, ϕ, $-\nu$, and α_c, when they are approximately constant over a range of k. Thus, we attempt to solve for these parameters over a range of c_k values; namely, $c_k, c_{k+1}, c_{k+2}, \ldots, c_{k+\mathrm{ws}}$, where **ws** is some prescribed integer. Over this specified window, we assume that $|A|, p, \eta, \phi, -\nu, \alpha_c$ are constant with respect to k. A system over this window can be constructed as follows:

$$\begin{pmatrix} 1 & \ln k & k \\ 1 & \ln(k+1) & k+1 \\ 1 & \ln(k+2) & k+2 \\ \vdots & \vdots & \vdots \\ 1 & \ln(k+\mathrm{ws}) & k+\mathrm{ws} \end{pmatrix} \begin{pmatrix} \ln|A| \\ -(p+1) \\ \eta \end{pmatrix} = \begin{pmatrix} \ln|c_k| \\ \ln|c_{k+1}| \\ \vdots \\ \ln|c_{k+\mathrm{ws}}| \end{pmatrix}, \tag{5.11}$$

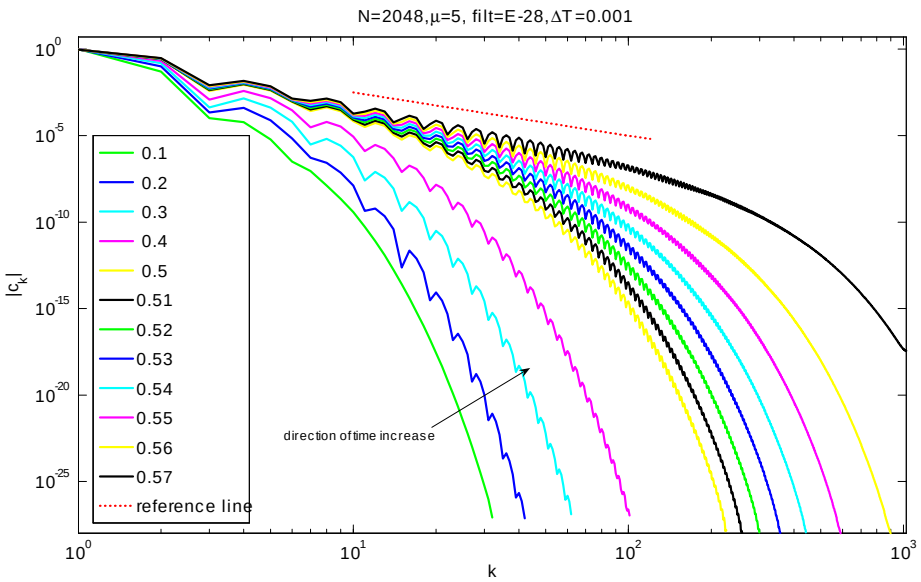

Figure 5.3: Fourier coefficients $|c_k|$ vs. k, for $\mu = 5$, with $\Gamma_T = 0$.. The dotted reference line denotes a slope of -2.5 on the plot. The coefficients increase as time increases.

$$\begin{pmatrix} 1 & \ln k & k \\ 1 & \ln(k+1) & k+1 \\ \vdots & \vdots & \vdots \\ 1 & \ln(k+\mathrm{ws}) & k+\mathrm{ws} \end{pmatrix} \begin{pmatrix} \phi \\ -\nu \\ -\alpha_c \end{pmatrix} = \begin{pmatrix} \tan^{-1}\left(\frac{y_k}{x_k}\right) \\ \tan^{-1}\left(\frac{y_{k+1}}{x_{k+1}}\right) \\ \vdots \\ \tan^{-1}\left(\frac{y_{k+\mathrm{ws}}}{x_{k+\mathrm{ws}}}\right) \end{pmatrix}. \tag{5.12}$$

We use the four-quadrant inverse tangent in matlab called **atan2** to compute $\tan^{-1}\left(\frac{y}{x}\right)$. This function returns values in the interval $[-\pi, \pi]$ (see matlab help for description). The correct 2π multiples need to be added to $\tan^{-1}\left(\frac{y}{x}\right)$ so that it increases smoothly; otherwise, we will get undue oscillations when we attempt to solve (5.12). Figures 5.4 and 5.5 plot the matlab function **atan2**$\left(\frac{y}{x}\right)$ without and with the 2π multiples added, respectively. $\tan_s^{-1}\left(\frac{y}{x}\right)$ is taken to denotes $\tan^{-1}\left(\frac{y}{x}\right)$ with the appropriate 2π multiple added. Thus, we actually seek to solve the following

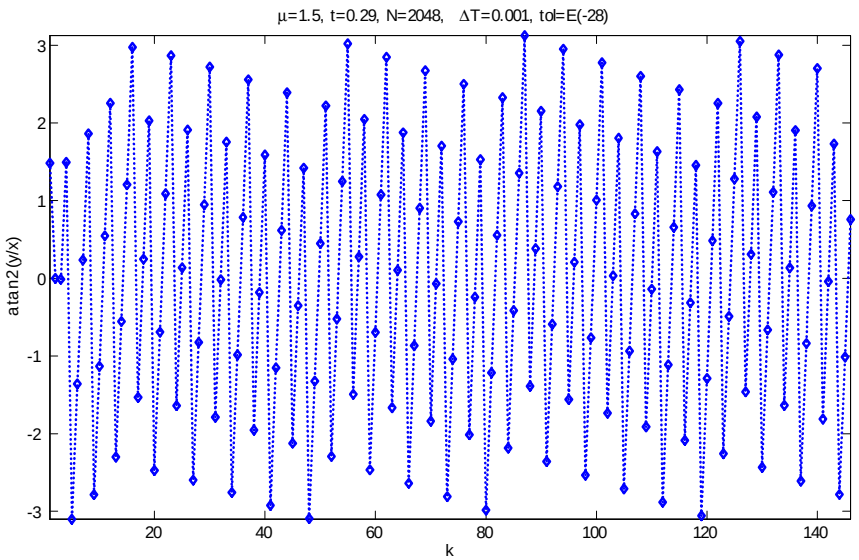

Figure 5.4: **atan2**$\left(\frac{y}{x}\right)$ vs. k.

system in lieu of (5.12):

$$\begin{pmatrix} 1 & \ln k & k \\ 1 & \ln(k+1) & k+1 \\ \vdots & \vdots & \vdots \\ 1 & \ln(k+\mathrm{ws}) & k+\mathrm{ws} \end{pmatrix} \begin{pmatrix} \phi \\ -\nu \\ -\alpha_c \end{pmatrix} = \begin{pmatrix} \tan_s^{-1}\left(\frac{y_k}{x_k}\right) \\ \tan_s^{-1}\left(\frac{y_{k+1}}{x_{k+1}}\right) \\ \vdots \\ \tan_s^{-1}\left(\frac{y_{k+\mathrm{ws}}}{x_{k+\mathrm{ws}}}\right) \end{pmatrix}. \tag{5.13}$$

5.3 Fitting Results

The systems (5.11) and (5.13) were solved in matlab by the \ command. Figures 5.6 and 5.7 show plots of the results for $\mu = 1.5, N = 2048$, $\Delta T = 0.001$, $l = 28$, and window size **ws** $= 5$. They were done for $t = 0.275,\ 0.28,\ 0.285, 0.29$. These times are close, and less than, the kink estimated critical time. Small changes in **ws** did not have a significant effect upon the results. The values of $|A|$, ϕ, and ν do not yield much significant information. We are most interested in p,η, and α_c;

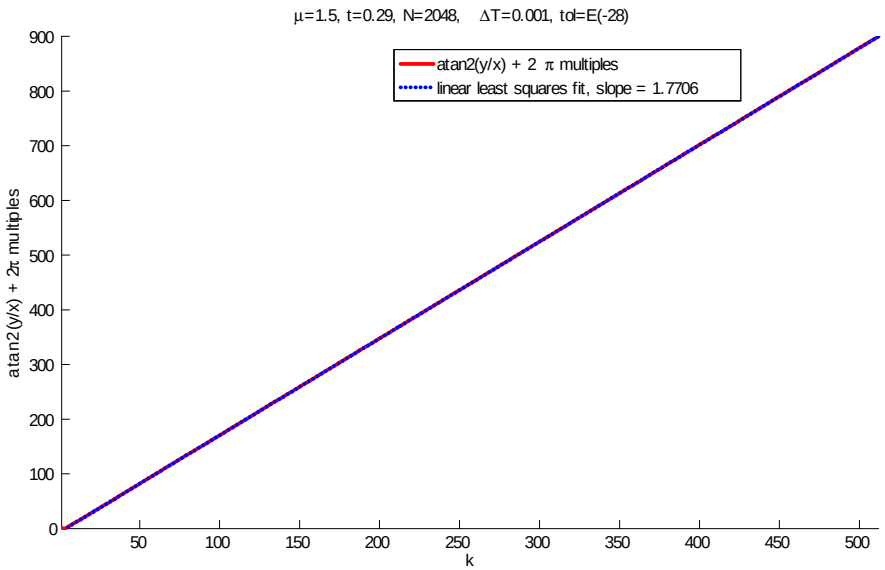

Figure 5.5: $\tan_s^{-1}\left(\frac{y}{x}\right)$ vs. k.

which support the occurrence of a branch point singularity in the lower complex α plane. The precision of p,η, and α_c is affected from a lack in total convergence in the parameters for large k. This noise for large k is due to the effect of the Fourier filter, truncation errors [19], and in the instance of increasing μ, possibly the role in the asymptotics of c_k due to the contribution from a second singularity formation. The first two given explanations could possibly be remedied by a further increase in the machine precision, the Fourier filter level, and the number of point vortices N. As such, we consider $20 \leq k \leq 200$.

In the Figure 5.6, we see that p roughly converges within the neighborhood of $\frac{3}{2}$, a value we would expect from the literature [24]. Recall that p is the order of the branch point singularity, as given in (5.7). α_c is the value of the Lagrangian parameter α when $\eta = 0$, and from which the location of the singularity on the sheet is known. α_c is the angle α associated with a specific infinitesimal part of the vortex

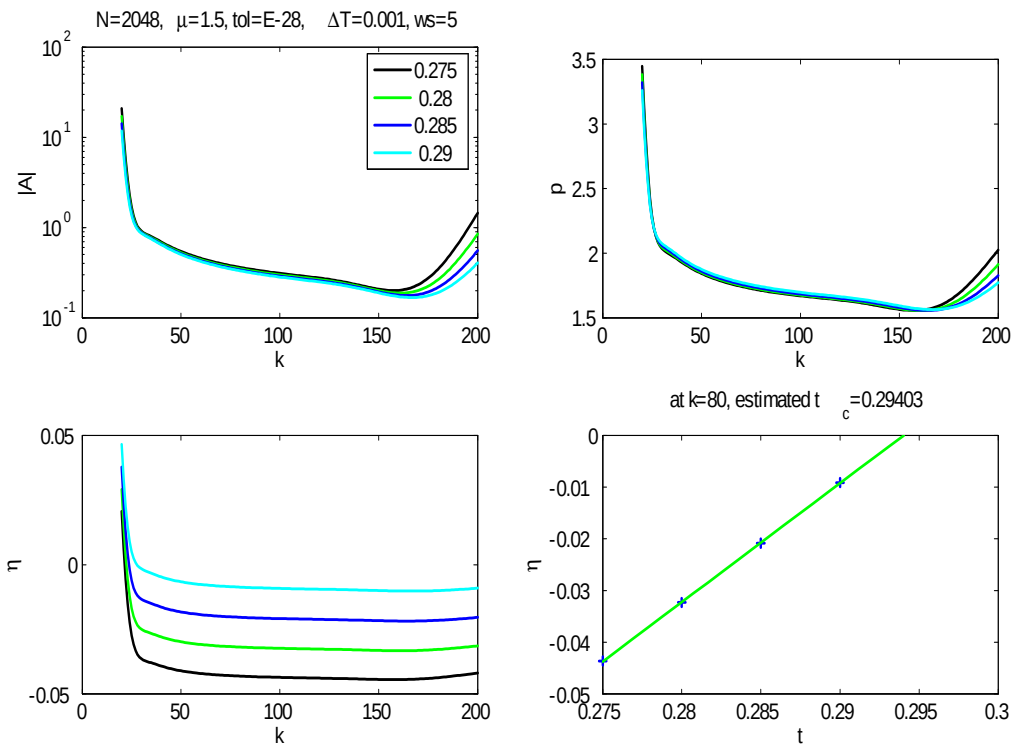

Figure 5.6: Parameters $|A|$, p, η in approximation (5.11), for $N = 2048$, $\Delta T = 0.001$, $l = 28$, $\Gamma_T = 0$, and $\mathbf{ws} = 5$.

sheet location at time zero; this specific infinitesimal part of the sheet moves to a different position from its original one as the sheet was evolved in time. Also, α_c is approximately negative the slope of $\tan_s^{-1}\left(\frac{y}{x}\right)$ vs. k, which was approximated with a linear least squares fit for $\mu = 1.5$ in Figure 5.5. Figure 5.7 gives $\alpha_c \approx -1.77$. This is in agreement with the value from the kink estimation, which was given in Figure 4.7 as $\alpha_c \approx -1.77$.[10] The time of singularity formation t_c can be estimated from how η approaches 0 for times prior to t_c. The bottom left subplot in Figure 5.6 shows this for when $k = 80$. It is important to take a value of k for which

[10]Note that Figure 4.7 actually given the estimate to be $\alpha_c \approx 4.51$. But this is equivalent to $\alpha_c \approx 2\pi - 4.51 \approx -1.77$.

η has approximately converged in k; values in the vicinity of $k = 80$ have a very mild affect upon this subplot. In this subplot, note that η is very close to being linear with respect to t. We take a linear least squares extrapolation to determine approximately the time at which $\eta = 0$. In this instance, it yields the estimate $t_c \approx 0.294$. Estimating t_c in this way shows that the t_c estimates via the kink and maximum curvature methods were slight overshoots of their actual values. For comparison, the kink estimate for $\mu = 1.5$, $N = 512$, $l = 28$ as previously given in Figure 4.6 is $t_c \approx 0.302$. Computations similar to those of Figures 5.6 and 5.7 were done for several values of μ. However; the fittings did not converge for μ large (i.e. $\mu \geq 5$).

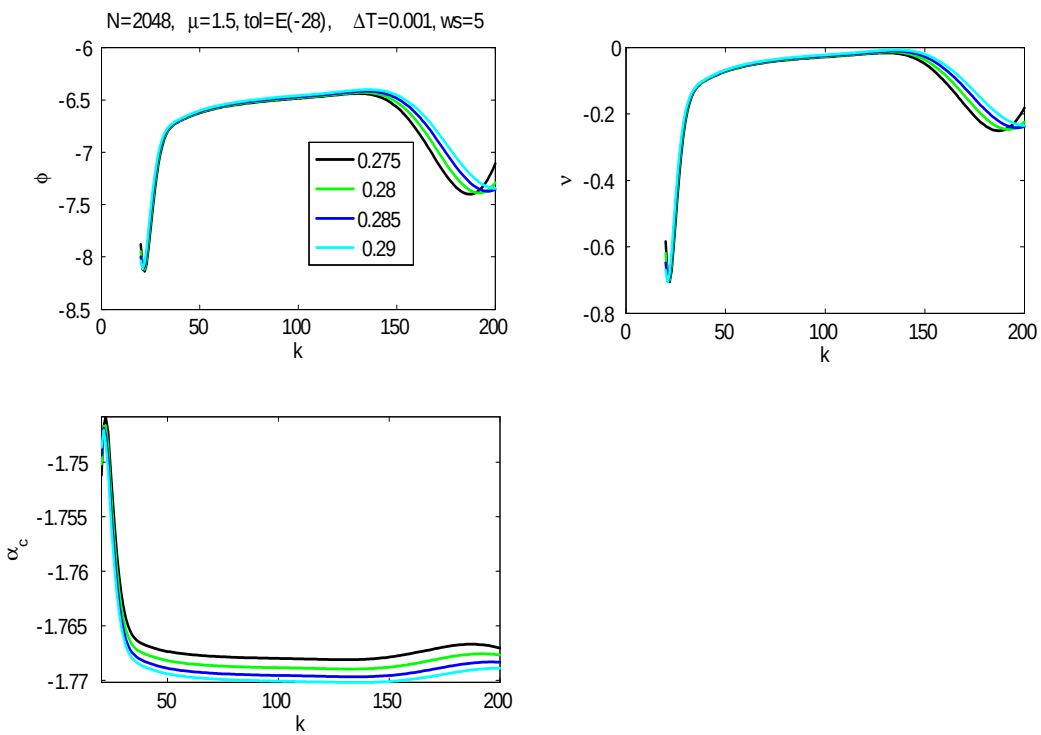

Figure 5.7: Parameters ϕ, ν, and α_c in approximation (5.12), for $N = 2048$, $\Delta T = 0.001$, $l = 28$, $\Gamma_T = 0$, and $\mathbf{ws} = 5$.

5.4 Second Singularity Formation

There is some indication that more than one singularity forms on each vortex sheet. These include the following:

1. The plots of the vortex sheets' geometries at their kink estimated critical times in Figure 4.4 show when Γ_T was changed from -5 to 5, the location of singularity formation changes from being on the the bottom half of the sheet to being on the top half. This change in location was also shown in Figure 4.7.

2. In the limiting case $\mu \to \infty$, it is known that two singularities occur simultaneously [24].

3. The oscillations in Fourier coefficients shown in Figures 5.2 and 5.3 increase as μ is increased (for $\Gamma_T = 0$). These increased oscillations approach the behavior of the Fourier spectrum in the limiting case $\mu \to \infty$, given in [24].

4. The fitting of the asymptotic parameters in Section 5.3 could not be applied the case of μ large.

5. In Chapter 6, it is shown that each vortex sheet rolls up into two double branched spirals for simulations[11] that go past the critical time.

We would like to use the techniques developed in Section 5.2 to gain more details of the second singularity formation, as were found in Section 5.3 for the first singularity formation. In order to do so, we apply a spatial smoothing to a prescribed neighborhood about the location of first singularity formation. The smoothing is done through a local application of either the evolution of the heat equation or a modified vortex blob method.

[11] These simulations use the vortex blob method.

5.4.1 Smoothing by the Heat Equation

Consider the one-dimensional heat equation without sources on a finite interval $\tilde{x}_0 < \tilde{x} < L$:

$$\begin{aligned} \frac{\partial u}{\partial t} &= \nu \frac{\partial^2 u}{\partial^2 \tilde{x}}, \\ u\left(\tilde{x}_0, t\right) &= u_0, \\ u\left(L, t\right) &= u_N, \\ u\left(\tilde{x}, 0\right) &= f\left(\tilde{x}\right). \end{aligned} \tag{5.14}$$

Define a uniform mesh given by $\tilde{x}_j = \tilde{x}_0 + j\Delta\tilde{x}$, where $j = 0, 1, 2, .., N$; and a time discretization by $t_m = m\Delta t$, $m = 0, 1, 2, .., M$. A forward time, centered spatial difference approximation of the heat equation is then given by:

$$u_j^{(m+1)} = u_j^{(m)} + s\left(u_{j+1}^{(m)} - 2u_j^{(m)} + u_{j-1}^{(m)}\right), \tag{5.15}$$

where $j = 1, 2, .., N-1$, m starts at 1, $u\left(\tilde{x}_j, t_m\right) \equiv u_j^{(m+1)}$, and $s = \nu\frac{\Delta t}{(\Delta\tilde{x})^2}$.[12] The constraint $0 < s <= \frac{1}{2}$ will guarantee that the numerical solution is stable [12].

Make $\nu \equiv \nu\left(\tilde{x}\right)$. Let $\nu_n\left(\tilde{x}\right) = (\tilde{x}-1)^n(\tilde{x}+1)^n$, for n even, and where $-1 \leq \tilde{x} \leq 1$; and

$$\sigma\left(\tilde{x}; p\right) = \begin{cases} \sigma_{\text{Erfc-Log}}\left(\left|\tilde{x}\right|; p\right), \text{ for } -1 \leq \tilde{x} < 0 \\ \sigma_{\text{Erfc-Log}}\left(\tilde{x}; p\right), \text{ for } 0 \leq \tilde{x} \leq 1 \end{cases},$$

[12] Note that N and Δt given here are not to be confused with the N and Δt pertaining to the number of point-vortices used in the point-vortex approximation and the timestep of the sheet evolution.

where $\sigma_{\text{Erfc-Log}}(\theta;p) \equiv \frac{1}{2}\text{erfc}\left\{2p^{\frac{1}{2}}\left(|\theta|-\frac{1}{2}\right)\sqrt{\frac{-\log\left[1-4\left(|\theta|-\frac{1}{2}\right)^2\right]}{4\left(|\theta|-\frac{1}{2}\right)^2}}\right\}$ as described in [1].[13] Figure 5.8 plots $\nu(\tilde{x})$ versus $\tilde{x}$ (top subplot) and their respective Fourier coefficients $|c_k|$ versus k (bottom subplot), for $\nu(\tilde{x}) = \nu_n(\tilde{x})$ and $\sigma(\tilde{x};p) = \nu_n(\tilde{x})$, where $n = 2, 4$ and $p = 2, 6, 12$. The legend entries n correspond to $\nu(\tilde{x}) = \nu_n(\tilde{x})$, and those including the erfclog terms correspond to $\nu(\tilde{x}) = \sigma(\tilde{x};p)$. The effect of increasing p can also be seen in Figure 5.8; in part, it will make the integrand of $\nu(\tilde{x})$ slimmer in a neighborhood about $\tilde{x} = 0$. Observe that as k increases beyond a small value (a little after $k = 10$ to be more precise), there will be sequentially larger decays in the Fourier coefficients $|c_k|$ of $\nu_2(\tilde{x})$, $\nu_2(\tilde{x})$, $\sigma(\tilde{x};6)$, and $\sigma(\tilde{x};12)$.

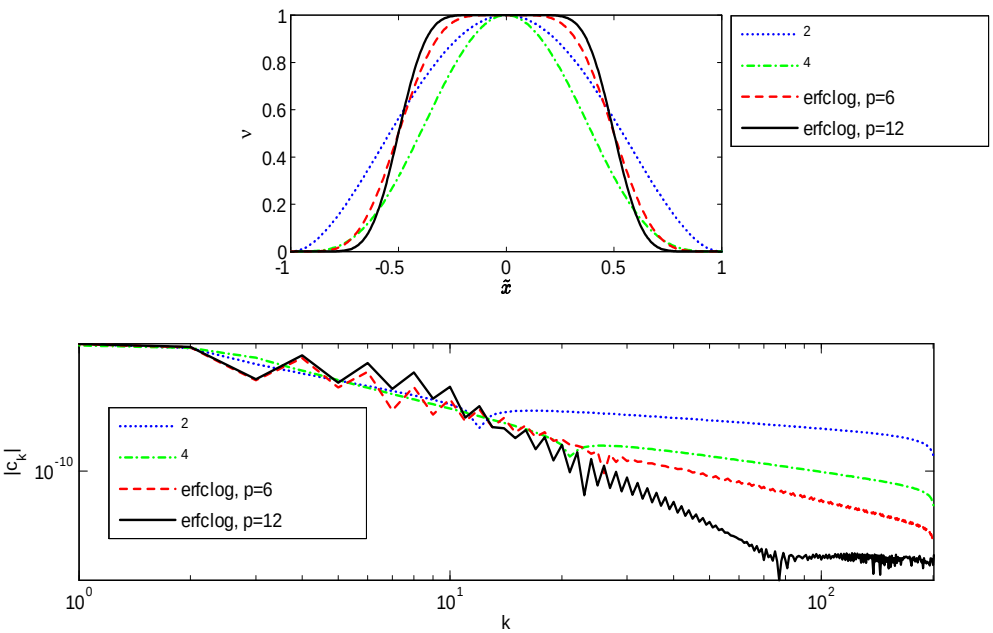

Figure 5.8: Plots of $\nu(\tilde{x})$ vs. $\tilde{x}$ and their respective Fourier coefficients $|c_k|$ vs. k, for several types of $\nu(\tilde{x})$ distributions.

[13]Note that this $\sigma(\tilde{x},t)$ is different than the $\sigma(s)$ corresponding to the vortex sheet strength mentioned earlier in the paper.

The heat equation is applied to both the x and y positions of the point vortices used in the vortex sheet approximation. As such, we will solve (5.15) for both of the cases $u = x$ and $u = y$. We let $\tilde{x} = kk$ in both cases, where kk is taken to be the discretization index corresponding to a specific point-vortex.[14] The smoothing is done in an index neighborhood h about the estimated location of the singularity that is intended to be smoothed. Furthermore, we impose a number of points h_0 on each side of the prescribed $\nu(\tilde{x})$ distribution for which we have additionally set $\nu(\tilde{x}) = 0$. Let

$$\nu_{\text{erf-logc, p}}(\tilde{x}) \equiv \begin{cases} 0, \text{ for } 0 \leq \tilde{x} \leq h_0 \\ \sigma\left(\left|\frac{\tilde{x}-h}{h-h_0}\right|; p\right), \text{ for } h_0 \leq \tilde{x} \leq h \\ \sigma\left(\frac{\tilde{x}-h}{h-h_0}; p\right), \text{ for } h \leq \tilde{x} \leq 2h - h_0 \\ 0, \text{ for } 2h - h_0 < \tilde{x} \leq 2h \end{cases} . \tag{5.16}$$

See the top plot in Figure 5.9 for an example of h, h_0, and $\nu(\tilde{x})$. For this example, $\nu(\tilde{x}) = \nu_{\text{erf-logc, 12}}(\tilde{x})$. $\max(s_u) = \max\left(\nu(\tilde{x})\frac{\Delta t}{(\Delta\tilde{x})^2}\right) = \max\left(\nu(k)\frac{\Delta t}{(\Delta k)^2}\right)$, where u can be taken to be either $u = x$ or $u = y$. Unless otherwise stated, $\max(s_x) = \max(s_y)$ since the same $\Delta\tilde{x}$ and Δt were typically used for the smoothings in both the x and y positions. This smoothing was applied to both of the following cases (and their outcomes given):

1. Over a neighborhood of the second singularity formation in an attempt to study the first singularity formation for μ large; namely, for μ large enough that the fitting methods developed in the Section 5.2 could not be applied. For these instances, we took the estimated location of the second singularity formation to be approximately equal to that of the limiting case $\mu \to \infty$ already

[14] This kk is not to be confused with the k corresponding to the index of the Fourier coefficients c_k.

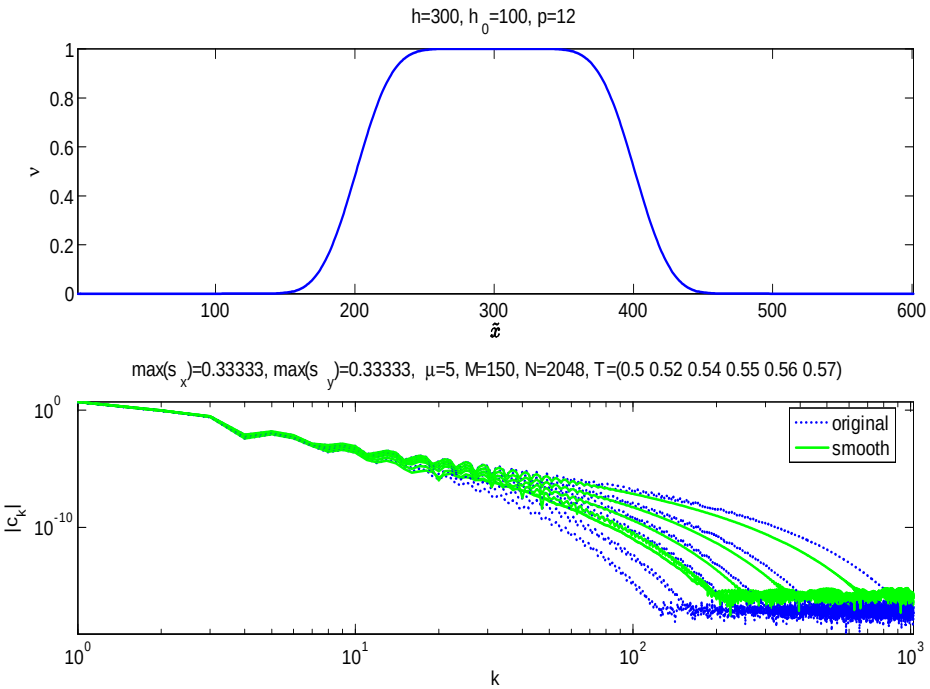

Figure 5.9: ν distribution (top plot) and Fourier coefficients of the vortex sheet position $|c_k|$ vs. k (bottom plot) before and after the smoothing was applied to a neighboorhood about the estimated location of the 1st singularity formation.

determined by Nitsche [24]. This case was also used to test the success of the smoothing on our vortex sheet problem. If this case of smoothing over the second singularity formation is successful, and the asymptotic parameters from Section 5.3 relating to the first singularity can then be determined, they should be similar to those in the limiting case $\mu \to \infty$ given by Nitsche. $\mu = 5$ was one of our test cases. Figure 5.9 plots the implemented $\nu(\tilde{x}) = \nu(\tilde{x}) = \nu_{\text{erf-logc, 12}}(\tilde{x})$ (where $h_0 = 100$, $h = 300$, and $p = 12$) distribution (top plot) and Fourier coefficients of the vortex sheet position $|c_k|$ vs. k (bottom plot) before and after the smoothing was applied to a neighborhood h about the estimated location of the first singularity formation. We set $M = 150$, $N = 2048$, and

performed the smoothing for $t = 0.5, 0.52, 0.54, 0.55, 0.56, 0.57$. Applying the methods in the Section 5.3 to the smoothed vortex sheet were not successful; the asymptotic system could not be solved via matlab.

2. Over a neighborhood of the first singularity formation in an attempt to determine the asymptotic parameters developed in Section 5.3 corresponding to the second singularity formation. In this case, the location of the first singularity formation was known for μ not large (i.e. $\mu \leq 2$), as determined in the Section 5.3. In the instances we attempted, including $\mu = 1.5$, $\mu = 2$, and other values of μ for which $\mu \leq 2$), the smoothing also did not yield any significant results with respect to determining the asymptotic parameters of the second singularity formation.

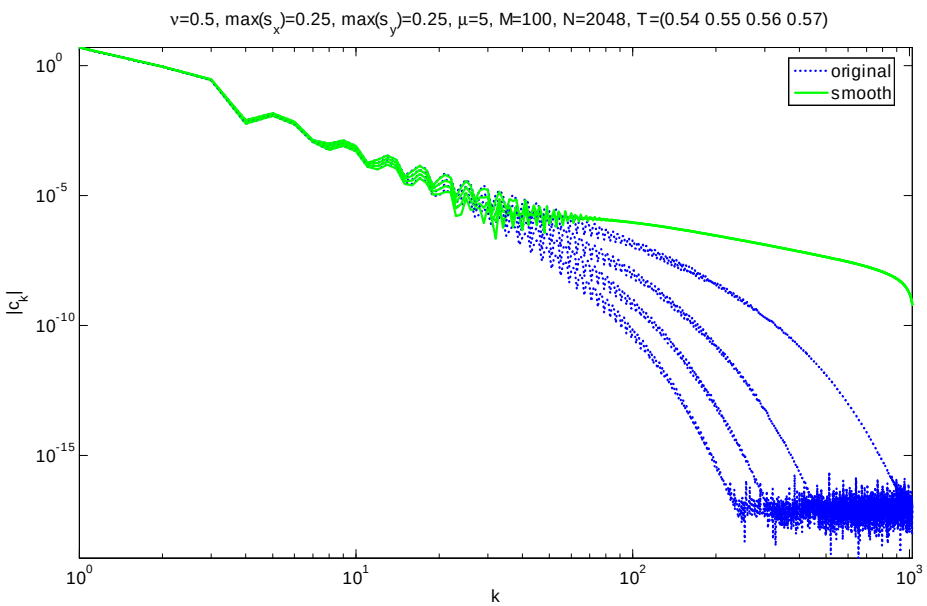

Figure 5.10: Fourier coefficients of the vortex sheets' position $|c_k|$ vs. k after the smoothing was applied, with $\nu = \frac{1}{2}$.

In both of these cases, it was important to apply the smoothing within an appro-

priate neighborhood about the designated singularity so that the smoothing does not affect the other singularity formation in question. In the smoothings implemented, attempts were performed for $\nu(\tilde{x}) = \nu_{\text{erf-logc, p}}(\tilde{x})$ and $\nu(\tilde{x}) = \nu_{\text{n}}(\tilde{x})$, for several n and p values ranging from 2 to 12. Several different values of the total number of timesteps M, Δt, h, and h_0; and consequently, various values of $\max(s) \leq \frac{1}{2}$ were used. These did not improve our sought after results.

As another last test case for this method, we smoothed over the entire vortex sheet with $\nu(\tilde{x}) = \frac{1}{2}$ to gain further insight into the effect of the smoothing. Figure 5.10 shows the Fourier coefficients the vortex sheet position $|c_k|$ vs. k before and after this smoothing was applied. Observe that $|c_k|$ corresponding to the smoothed data decays less for large k that corresponding to the non-smoothed $|c_k|$. This shows that the actual attempt to sufficiently smooth the positions of the vortex sheet was not successful.

Possible explanations for the failure of the implementation to yield smoother results include error in the modes introduced by the discretization, and $\nu(\tilde{x})$ not being sufficiently smooth in its discretization.

5.4.2 Smoothing with the Vortex Blob Method

We again consider smoothing over a portion of the vortex sheet, but this time using a variation of the vortex blob method mentioned in Section 2.2.2. In (2.6), let $\delta \equiv \delta(\alpha)$. Then (2.6) becomes

$$\begin{aligned}\mathbf{u}(\mathbf{x},t) &= \frac{1}{2\pi}\int_0^{2\pi}\frac{1}{(x-\tilde{x})^2+(y-\tilde{y})^2+\delta(\alpha)^2}\begin{pmatrix}\tilde{y}-y\\ x-\tilde{x}\end{pmatrix}\sigma(\alpha)\ d\alpha \quad (5.17)\\ &\quad +\frac{1}{2\pi}\int_0^{2\pi}\frac{1}{(x-\tilde{x})^2+(y+\tilde{y})^2+\delta(\alpha)^2}\begin{pmatrix}y+\tilde{y}\\ \tilde{x}-x\end{pmatrix}\sigma(\alpha)\ d\alpha.\end{aligned}$$

Now, choose

$$\delta_n(\alpha)\equiv\begin{cases}0, \text{ if } \alpha<\alpha_j-\varepsilon\\ \delta_{\max}(-\frac{\alpha-\alpha_j-\varepsilon}{\varepsilon})^n(\frac{\alpha-\alpha_j+\varepsilon}{\varepsilon})^n, \text{ if } \alpha_j-\varepsilon\le\alpha\le\alpha_j+\varepsilon\\ 0, \text{ if } \alpha_j+\varepsilon<\alpha\end{cases}. \quad (5.18)$$

So, within an ε neighborhood about α_j, a modified vortex blob method is implemented. We choose α_j to be equal to the estimated α_c value corresponding to the location of the singularity to be smoothed. $\delta_{\max}$ was taken to be either 0.1 or 0.2. For this method, we replaced the integral approximation methods with correction terms as described in Section 3.1 with a method used by Shelley [26], termed the modified point-vortex approximation, which does not include the use of the correction terms, but is also exponentially accurate. This made coding this problem more convenient. The vortex sheets' were evolved according to (5.17), the implementation of the Fourier filter. Still, noise was prevalent in the geometries of the vortex sheets. As time was incremented, it arose to the extent that it significantly perturbed the evolution of the vortex sheets' positions. This attempt of a smoothing proved unsuccessful. As a test case, we tried changing $\delta_n(\alpha)$ as given in (5.17) to a periodic function $\delta_n(\alpha)=\delta_{\max}\sin^2(\alpha-\alpha_j)$ for $\delta_n(\alpha)=\delta_{\max}\cos^2(\alpha-\alpha_j)$ to see if it would improve the problem of the noise. It was hoped that if a periodic function was useful in decreasing the noise, we could adjust it so that its magnitude is small

away from the first singularity formation, and larger near the location of the second singularity formation. The periodic functions mentioned, however, did not result in an improvement.

Chapter 6

Evolution Past Critical Times

Thus far, we have performed evolutions of the vortex sheets up only to their estimated critical times. As mentioned in Section 2.2.2, with the use of the vortex blob method, according to (2.6), the vortex sheets can be evolved past their estimated critical times, with an appropriate choice of δ. Suitable choices include, for example, $\delta = 0.2, 0.1$,or 0.05. Figure 6.1 plots the vortex sheet evolutions with $\mu = 5$, $\delta = 0.1$, $\Delta T = 0.01$, and for $\Gamma_T = -5, 0, 5$. Recall that the vortex sheets are prescribed an initial velocity $\mathbf{U} = (1, 0, 0)$. Note that the value of Γ_T determines the location of the first singularity formation, as well as which portion of the vortex sheet rolls up first. Nitsche [23] studied the vortex sheet roll-up for a single initially cylindrical vortex sheet with $\Gamma_T = 0$, which is our limiting case $\mu \to \infty$. The middle set of plots in the figure for $\mu = 5$, $\Gamma_T = 0$, is in close agreement to those results, as they should be. Figure 6.2 plots the computed top vortex sheets again with $\delta = 0.1$, $\Delta T = 0.01$, and $\Gamma_T = -5, 0, 5$, but now with $\mu = 1.5$. The three plots in the top right corner corresponding to $T = 4, \Gamma_T = -5$; $T = 6, \Gamma_T = -5$; and $T = 6, \Gamma_T = 0$ appear to have a portion of their vortex sheets touching the x-axis. This would imply that the top vortex sheets are actually touching the bottom vortex sheets at those times. Also, observe that for the middle set of plots in the figure, $\mu = 1.5$, $\Gamma_T = 0$, the top

and bottom halves of the top vortex sheet do not roll up as symmetrically as in the case for $\mu = 5$, $\Gamma_T = 0$ given in Figure 6.1.

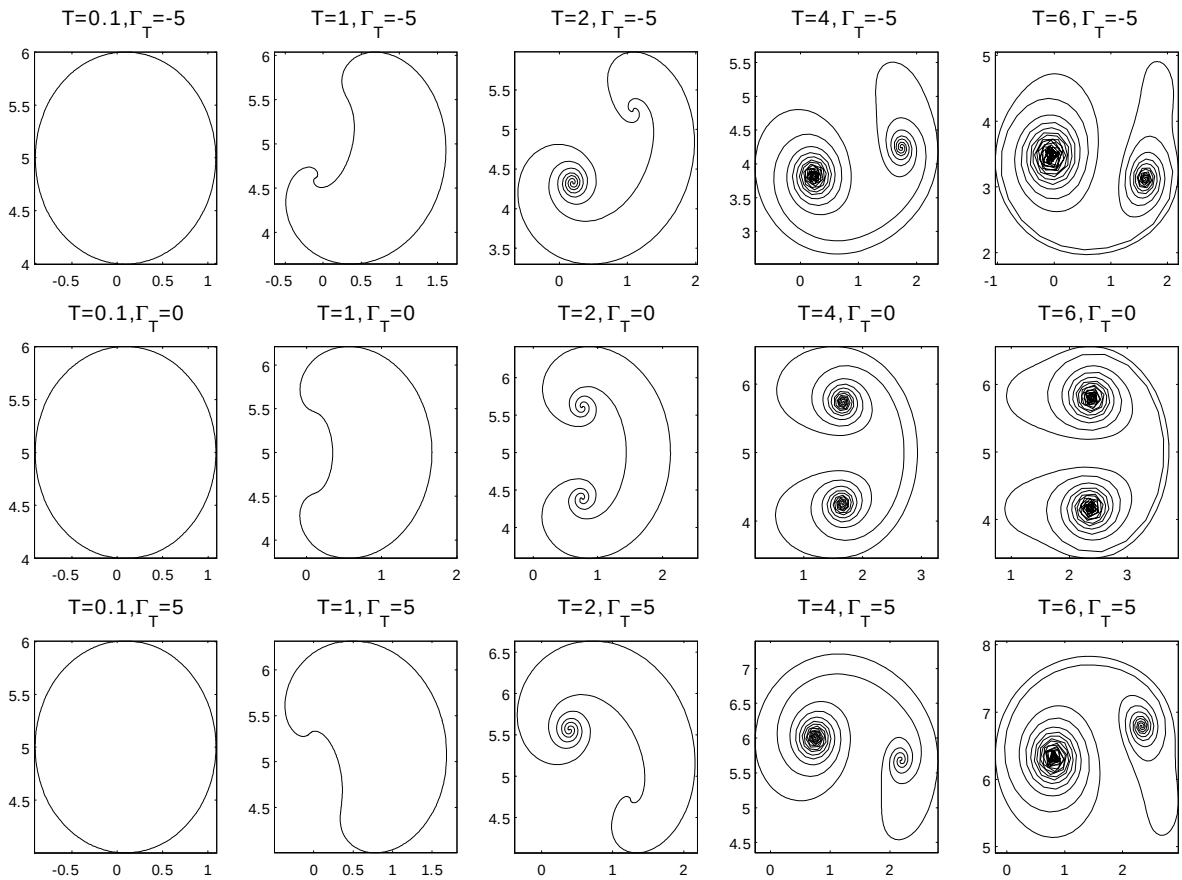

Figure 6.1: Computed top vortex sheets using the vortex blob method, for $\mu = 5$, $\delta = 0.1$, $\Delta T = 0.01$, and with $\Gamma_T = -5, 0, 5$.

A few comments are in order regarding the lift forces on the vortex sheets. According to [5, p. 93], the Kutta-Joukowski Theorem states the following: "Consider incompressible potential flow exterior to a region B. Let the velocity field approach the constant value $(U, V) = \mathbf{U}$ at infinity. Then the force exerted on B is given by $F = -\rho\Gamma_T \|\mathbf{U}\| \mathbf{n}$, where Γ_T is the circulation around B and $\mathbf{n}$ is a unit vector

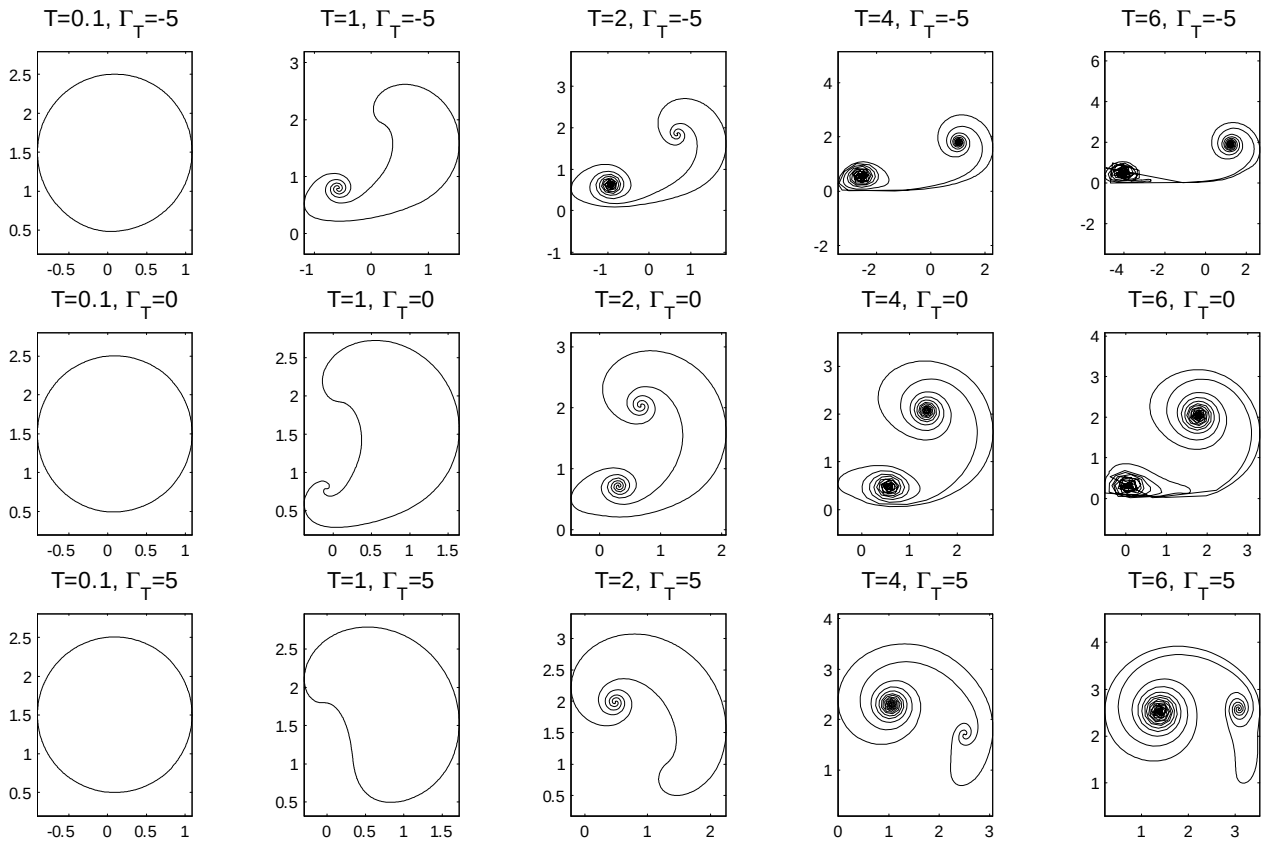

Figure 6.2: Computed top vortex sheets using the vortex blob method, for $\mu = 1.5$, $\delta = 0.1$, $\Delta T = 0.01$, and with $\Gamma_T = -5, 0, 5$.

orthogonal to $\mathbf{U}$." The Kutta-Joukowski Theorem can be applied to the top vortex sheet[1], for example, in the limiting case $\mu \to \infty$. For $\Gamma_T = 0$, there is no net force

[1]For these considerations, to make $\|\mathbf{U}\|$ nonzero for the flow, we simply change our reference frame as follows: Choose the initial velocity inside the vortex sheets to be $(0, 0, 0)$. The velocity field outside the vortex sheets would then be changed by subtracting U from the previously $\hat{\mathbf{x}}$ directed velocity field component for outside the vortex sheets. In that case, the flow far away from the vortex sheets would become a uniform rectilinear flow described by the velocity field $(-U, 0, 0)$. And initially, the flow would then be analogous to a $-\hat{\mathbf{x}}$ directed uniform rectilinear flow of magnitude U past the two vortex sheets.

acting on the vortex sheet, and thus no drag (recall d'Alembert's paradox). An application of the Kutta-Joukowski Theorem often noted is that for uniform flow past a single cylinder with circulation [11] [8].

The Kutta-Joukowski Theorem cannot, however, be applied to a single vortex sheet in our problem for μ finite. But, it can be applied to determine the total force summed from that due to both of the vortex sheets [8]. Nevertheless, due to our prescribed symmetry of the vortex sheets, (i.e. the bottom vortex sheet is a reflection about the x-axis of the top vortex sheet), the total sum of circulation summed from the top and bottom vortex sheets will be 0. The bottom vortex sheet will have a negative circulation, but of the same magnitude, of that of the top vortex sheet. If one wished to prescribe the top and bottom vortex sheets with individual circulations with different magnitudes, or same signs, one would need to change the initial setup of the problem, and break the symmetry we imposed on the two vortex sheets. For our problem in question, due to the symmetry we prescribed on the vortex sheets, we know that the lift forces must be equal in magnitude and opposite in direction.

Even in the instance that each vortex sheet is prescribed a 0 circulation, there is a force of attraction between them. This is because when more than one body is moving through an ideal fluid, a mutual force is exerted between them (if they have no circulation, and possibly even if they do have circulation) [25, p. 109]. This force of attraction increases as μ becomes smaller. Further explanation of these concepts is discussed by Crowdy for the case of a finite stack of cylindrical airfoils in [8].

Chapter 7

Summary

The evolution of two initially cylindrical, counter-rotating vortex sheets was computed. Several values of both their non-dimensionalized separation distance μ, and total prescribed circulation Γ_T around each sheet were taken into consideration. More than one method was used to estimate their times and locations of the singularity formation. These include an analysis of the blow up in the maximum curvature $\boldsymbol{\kappa}$ of the sheets' geometries, the post-critical-time kink formation, and the transition from exponential to algebraic decay in the Fourier spectrum and the associated linear-least-squares fitting of the asymptotic parameters. The branch-point singularities were confirmed to be of order $\frac{3}{2}$.

Several indications were given for the presence of a second singularity formation in the vortex sheets, for μ finite. Smoothings the initial singularity formation were conducted using either the heat equation or a local application of the vortex blob method. It was hoped that doing so would allow one to determine the values of the asymptotic parameters, and hence, obtain the analogous asymptotic information that was gained in doing so with the first singularity formation. The smoothings were, however, unsuccessful towards this aim.

The vortex sheet roll-up past times of singularity formation was studied with the use of the vortex-blob method.

The evolution of the two cylindrical vortex problem could possibly be extended to the case of the evolution of a set of multiple initially cylindrical vortex sheets, with the aid the content found in [7] [8] [9], by providing a means for solve for the associated initial sheet strengths $\sigma(s)$.

Modelling the evolution of an initially toroidal vortex sheet is one of next logical extensions for the problem considered in this paper.

Chapter 8

Appendices

Appendix A

Non-dimensionalization

In this section, we show the non-dimensionalization of the initial conditions (2.1) to that of (2.2), as well as for that of the evolution equations (2.5). The end result will be the introduction of the parameter $\mu = \frac{D}{R}$ in lieu of using both D and R. This leads to a greater simplicity in the simulations of the given problem.

Let R and U be quantities with units of length and velocity, respectively. Let us introduce the following dimensionless quantities $\mathbf{U}^* = \frac{\mathbf{U}}{U} = \left(\frac{U}{U}, 0, 0\right) = (1, 0, 0)$. $\mathbf{x}^* = \frac{\mathbf{x}}{R}$, $\tilde{\mathbf{x}}^* = \frac{\tilde{\mathbf{x}}}{R}$, $\Gamma^* = \frac{\Gamma}{RU}$, and $t^* = \frac{U}{R}t$. So $R\mathbf{x}^* = \mathbf{x}$, $\frac{d\mathbf{x}}{d\mathbf{x}^*} = R$, $d\Gamma = RU\, d\Gamma^*$, and $\frac{dt^*}{dt} = \frac{U}{R}$. Then $R\mathbf{x}^* = \mathbf{x}(\alpha, t) = \begin{pmatrix} R\cos\alpha \\ D + R\sin\alpha \end{pmatrix}$ implies that $\mathbf{x}^* = \begin{pmatrix} \cos\alpha \\ \frac{D}{R} + \sin\alpha \end{pmatrix}$.

Also, $\frac{d\mathbf{x}(\alpha,t)}{dt} = \frac{d\mathbf{x}}{d\mathbf{x}^*}\frac{d\mathbf{x}^*}{dt} = R\frac{d\mathbf{x}^*}{dt} = R\frac{d\mathbf{x}^*}{dt^*}\frac{dt^*}{dt} = R\frac{U}{R}\frac{d\mathbf{x}^*}{dt^*} = U\frac{d\mathbf{x}^*}{dt^*}$. So

$\frac{d\mathbf{x}^*}{dt^*} = \frac{1}{U}\left[U\frac{d\mathbf{x}^*}{dt^*}\right] = \frac{1}{U}\frac{d\mathbf{x}(\alpha,t)}{dt}$

$= \frac{1}{2\pi U} P.V. \int_0^{2\pi} \frac{1}{(x-\tilde{x})^2+(y-\tilde{y})^2} \begin{pmatrix} \tilde{y} - y \\ x - \tilde{x} \end{pmatrix} \frac{d\Gamma}{d\tilde{\alpha}} d\tilde{\alpha}$

$$+\frac{1}{2\pi U}\int_0^{2\pi}\frac{1}{(x-\tilde{x})^2+(y+\tilde{y})^2}\begin{pmatrix} y+\tilde{y} \\ \tilde{x}-x \end{pmatrix}\frac{d\Gamma}{d\tilde{\alpha}}d\tilde{\alpha}$$

$$=\frac{1}{2\pi U}P.V.\int_0^{2\pi}\frac{1}{(Rx^*-R\tilde{x}^*)^2+(Ry^*-R\tilde{y}^*)^2}\begin{pmatrix} R\tilde{y}-Ry \\ Rx-R\tilde{x} \end{pmatrix}\frac{RU\ d\Gamma^*}{d\tilde{\alpha}}d\tilde{\alpha}$$

$$+\frac{1}{2\pi U}\int_0^{2\pi}\frac{1}{(Rx^*-R\tilde{x}^*)^2+(Ry^*+R\tilde{y}^*)^2}\begin{pmatrix} Ry+R\tilde{y} \\ R\tilde{x}-Rx \end{pmatrix}\frac{RU\ d\Gamma^*}{d\tilde{\alpha}}d\tilde{\alpha}$$

$$=\frac{R^2U}{2\pi R^2U}P.V.\int_0^{2\pi}\frac{1}{(x^*-\tilde{x}^*)^2+(y^*-\tilde{y}^*)^2}\begin{pmatrix} \tilde{y}-y \\ x-\tilde{x} \end{pmatrix}\frac{d\Gamma^*}{d\tilde{\alpha}}d\tilde{\alpha}$$

$$+\frac{R^2U}{2\pi R^2U}\int_0^{2\pi}\frac{1}{(x^*-\tilde{x}^*)^2+(y^*+\tilde{y}^*)^2}\begin{pmatrix} y+\tilde{y} \\ \tilde{x}-x \end{pmatrix}\frac{d\Gamma^*}{d\tilde{\alpha}}d\tilde{\alpha}$$

$$=\frac{1}{2\pi}\int_0^{2\pi}\frac{1}{(x^*-\tilde{x}^*)^2+(y^*-\tilde{y}^*)^2}\begin{pmatrix} \tilde{y}-y \\ x-\tilde{x} \end{pmatrix}\frac{d\Gamma^*}{d\tilde{\alpha}}d\tilde{\alpha}$$

$$+\frac{1}{2\pi}\int_0^{2\pi}\frac{1}{(x^*-\tilde{x}^*)^2+(y^*+\tilde{y}^*)^2}\begin{pmatrix} y+\tilde{y} \\ \tilde{x}-x \end{pmatrix}\frac{d\Gamma^*}{d\tilde{\alpha}}d\tilde{\alpha}.$$

Thus, the governing equations $\frac{d\mathbf{x}^*}{dt^*}$ are the same as those for $\frac{d\mathbf{x}}{dt}$, where $\mathbf{x}^* = \begin{pmatrix} \cos\alpha \\ \frac{D}{R}+\sin\alpha \end{pmatrix}$. Let $\mu \equiv \frac{D}{R}$. And for simplicity, let us now drop the $*$ so that $\mathbf{x}^*$ becomes $\mathbf{x}$, etc. Then we have

$$\mathbf{x}(\alpha) = \begin{pmatrix} x(a) \\ y(a) \end{pmatrix} = \begin{pmatrix} \cos\alpha \\ \mu+\sin\alpha \end{pmatrix}. \tag{A.1}$$

See Figure 2.2 for a schematic of this description. And, the initially prescribed velocity of the vortex sheets and the fluid contained within the vortex sheets now becomes $\mathbf{U} = (1, 0, 0)$.

Appendix B

Asymptotics of the Fourier Integral for c_{-k}

This section is similar to that done in of Section 5.1, but pertains to the asymptotics of c_{-k}. The more significant steps of this derivation are given in by Carrier, Krook, and Pearson [3, p. 255-56]. Consider the Fourier integral $I(k) = \int_{-\infty}^{\infty} e^{ikz} f(z)\ dz$, $k \in \mathbb{N}$, where the path of integration is the same as that previously. Suppose that in a neighborhood of ζ_j,

$$f(z) = \left(z - \zeta_j\right)^{\nu} \sum_{n=0}^{\infty} a_n \left(z - \zeta_j\right)^n, \tag{B.1}$$

with $\operatorname{Re} \nu > -1$, and $|f(z)| \to 0$ uniformly as $z \to \infty$. Again by using Jordan's lemma and the Cauchy-Goursat theorem,

$$I(k) = \int_{\Upsilon_1 + \Upsilon_2} e^{ikz} f(z)\ dz. \tag{B.2}$$

Appendix B. Asymptotics of the Fourier Integral for c_{-k}

The contribution from Υ_j to $I(k)$ is given by

$$\begin{aligned}
I_{\Upsilon_j}(k) &= \int_{\Upsilon_j} e^{ikz}\left(z-\zeta_j\right)^{\nu}\left[\sum_{n=0}^{\infty} a_n\left(z-\zeta_j\right)^n + R_N(z)\right]\,dz \\
&= \int_{\Upsilon_{j_{\text{down}}}} e^{ikz}\left(z-\zeta_j\right)^{\nu}\left[\sum_{n=0}^{\infty} a_n\left(z-\zeta_j\right)^n + R_N(z)\right]\,dz \\
&\quad + \int_{\Upsilon_{j_{\text{up}}}} e^{ikz}\left(z-\zeta_j\right)^{\nu}\left[\sum_{n=0}^{\infty} a_n\left(z-\zeta_j\right)^n + R_N(z)\right]\,dz \\
&= -\int_0^{\infty} e^{ik\left(\zeta_j+ir\right)}e^{-i\frac{3\pi}{2}\nu}r^{\nu}\left[\sum_{n=0}^{\infty} a_p i^n r^n + R_N\left(\zeta_j+ir\right)\right] i\,dr \\
&\quad + \int_0^{\infty} e^{ik\left(ir+\zeta_j\right)}e^{i\frac{\pi}{2}\nu}r^{\nu}\left[\sum_{n=0}^{\infty} a_p i^n r^n + R_N\left(\zeta_j+ir\right)\right] i\,dr \qquad \text{(B.3)} \\
&= i\left(e^{i\frac{\pi}{2}\nu}-e^{-i\frac{3\pi}{2}\nu}\right)e^{ik\zeta_j}\int_0^{\infty} e^{-kr}r^{\nu}\left[\sum_{n=0}^{\infty} a_n i^n r^n + R_N\left(\zeta_j+ir\right)\right]\,dr \\
&= -2\frac{\left(e^{i\pi\nu}-e^{-i\pi\nu}\right)}{2i}e^{-i\frac{\pi}{2}\nu}e^{ik\zeta_j}\int_0^{\infty} e^{-kr}r^{\nu}\left[\sum_{n=0}^{\infty} a_p i^n r^n + R_N\left(\zeta_j+ir\right)\right]\,dr \\
&= -2\sin(\pi\nu)\,e^{\left(ik\zeta_j-i\frac{\pi}{2}\nu\right)}\int_0^{\infty} e^{-kr}r^{\nu}\left[\sum_{n=0}^{\infty} a_p i^n r^n + R_N\left(\zeta_j+ir\right)\right]\,dr,
\end{aligned}$$

where we let $z=\zeta_j+ir$. Then by Watson's lemma, for $|k|$ large we have

$$I_{\Upsilon_j}(k) \sim -2\sin(\pi\nu)\,e^{\left(ik\zeta_j+i\frac{\pi}{2}\nu\right)}\sum_{n=0}^{\infty} a_n i^n\frac{\Gamma(\nu+n+1)}{k^{\nu+n+1}}. \qquad \text{(B.4)}$$

For $|k|$ large, $I(k)$ is dominated by the particular $I_{\Upsilon_j}(k)$ with the smallest[1] $\operatorname{Im}\zeta_j$. This can easily be seen by considering the dominant term $e^{ik\zeta_j}=e^{ik\operatorname{Re}\left(\zeta_j\right)}e^{-k\operatorname{Im}\left(\zeta_j\right)}$ in the above expression. So

$$I(k) \sim -2\sin(\pi\nu)\,e^{\left(ik\tilde{z}-i\frac{\pi}{2}\nu\right)}\sum_{n=0}^{\infty} a_n i^n\frac{\Gamma(\nu+n+1)}{k^{\nu+n+1}}, \qquad \text{(B.5)}$$

[1] 'smallest' is not to be taken in the $\left|\operatorname{Im}\zeta_j\right|$ sense. For example, if $\forall j$, $\zeta_j>0$, then the ζ_j with 'smallest' imaginary part would be the one with least positive value.

where $\tilde{z}$ is now the particular ζ_j with smallest imaginary part, assuming such a $\tilde{z}$ exists. Again by letting $n = 0$, we then have

$$I(k) \sim -\frac{2a_0 \sin(\pi\nu)\,\Gamma(\nu+1)}{k^{\nu+1}} e^{\left(ik\tilde{z} - i\frac{\pi}{2}\nu\right)}. \tag{B.6}$$

In this work, we performed the fitting of asymptotic parameters to that of c_k. The asymptotics for c_{-k} were included so that one could do similar fittings for c_{-k} if desired.

References

[1] Boyd, J. P. The Erfc-Log Filter and the Asymptotics of the Euler and Vandeven Sequence Accelerations. *Houston J. Math.*, Houston. 267-276 (1996).

[2] Caflisch, R. E., Hou, T. Y., Lowengrub. Almost Optimal Convergence of the Point Vortex Method for Vortex Sheets Using Numerical Filtering. *Math. Comput.* 68 (228), 1465-1496 (1999).

[3] Carrier, Krook, Pearson. Functions of a Complex Variable. Mcgraw-Hill, New York, 1966.

[4] Chorin, A. J., Bernard, P. S. Discretization of a Vortex Sheet, with an Example of Roll-up. *J. Comput. Phys.* 13, 423-429 (1973).

[5] Chorin, J. C., Marsden, J. E. A Mathematical Introduction to Fluid Mechanics, 3rd ed. Springer, New York, 2000.

[6] Crowdy, Darren. A New Calculus for Two-dimensional Vortex Dymanics. *Theor. Comput. Fluid Dyn.* 24, 9-24 (2010).

[7] Crowdy, Darren. Analytical Solutions for Uniform Potential Flow Past Multiple Cylinders. *Eur. J. Mech. B. Fluids.* 25, 459-470 (2006).

[8] Crowdy, Darren. Calculating the Lift on a Finite Stack of Cylindrical Aerofoils. *Proc. R. Soc. A.* 426, 1387-1407 (2006)

[9] Crowdy, Darren. Computing the Schottky-Klein Prime Function on the Schottky Double of Planar Domains. *Comput. Methods Funct. Theory.* 7, 293-308 (2007)

[10] Cowley, S. Baker, G. Tanveer, S. On the Formation of Moore Curvature Singularities in Vortex Sheets. *J. Fluid Mech.* 378, 233-267 (1999).

[11] Currie, I. E. Fundamental Mechanics of Fluids. CRC Press, Toronto. 2003.

[12] Haberman, R. Applied Partial Differential Equations with Fourier Series and Boundary Value Problems. Pearson Prentice Hall, Upper Saddle River, NJ, 2004.

[13] Krasny, R. A Study of Singularity Formation in a Vortex Sheet by the Point-vortex Approximation. *J. Fluid Mech.* 167, 65-93 (1986).

[14] Krasny, R. Desingularization of Periodic Vortex Sheet Roll-up. *J. Comp. Phys.* 65 (2), 292-313 (1988).

[15] Lindsay, K., Krasny, R. A Particle Method and Adaptive Treecode for Vortex Sheet Motion in Three-Dimensional Flow. *J. Comp. Phys.* 172, 879-907 (2001).

[16] Lagally, M. *Die Reibungslose Strömung im Aussengebiet Zweier Kreise.* A. Angew. Math. Mech. 9, 299-305 (1929).

[17] Meyer, R. Introduction to Mathematical Fluid Dynamics. Dover, New York, 1971.

[18] Moore, D. W. The Spontaneous Appearance of a Singularity in the Shape of an Evolving Vortex Sheet. *Proc. R. Soc. London. A.* 365, 105-119 (1979).

[19] Nie, Q., Baker, G. Application of Adaptive Quadrature to Axi-symmetric Vortex Sheet Motion. *J. Comp. Phys.* 143, 49-69 (1998).

[20] Netlib routine. http://www.netlib.org/slatec/src/hfti.f.

[21] Nitsche, M. Axisymmetric Vortex Sheet Motion: Accurate Evaluation of the Principal Value Integral. S*IAM J. Sci. Comput.* 21 (3), 1066-1084 (1999).

[22] Nitsche, M. Math 471: Introduction to Scientific Computing. Course Notes. University of New Mexico, 2006.

[23] Nitsche, M. Self-similar Shedding of Vortex Rings. *J. Fluid. Mech.* 435, 397-407 (2001).

[24] Nitsche, M. Singularity Formation in a Cylindrical and a Spherical Vortex Sheet. *J. Comput. Phys.* 173, 208-230 (2001).

[25] Prandtl, L., Tietjens, O. G. Applied Hydo- and Aeromechanics. Dover, New York, 1934.

[26] Shelley, M. J. A study of Singularity Formation in Vortex-sheet Motion by a Spectrally Accurate Vortex Method. *J. Fluid Mech.* 244, 493-526 (1992).

[27] Sulem, C. Lulem, P.L., Frisch, H. Fracing Complex Singularities with Spectal Methods. *J. Comp. Phys.* 50, 138-161 (1983).

[28] van de Vooren, A. I. A Numerical Investigation of the Rolling-up of Vortex Sheets. *Proc. R. Soc. Lond.* 373, 67-91 (1980).